J. Fluid Mech. (2021), *vol*. 915, A26, doi:10.1017/jfm.2021.84

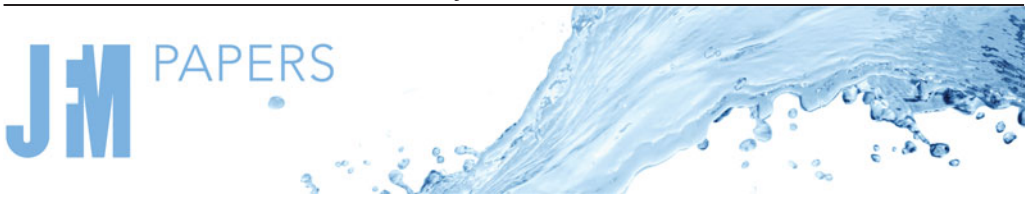

Instabilities and transition in cooled wall hypersonic boundary layers

S. Unnikrishnan[1],† **and Datta V. Gaitonde**[2]

[1]Mechanical Engineering, Florida State University, Tallahassee, FL 32310, USA

[2]Mechanical and Aerospace Engineering, The Ohio State University, Columbus, OH 43210, USA

(Received 24 May 2020; revised 8 November 2020; accepted 25 January 2021)

Wall cooling has substantial qualitative and quantitative effects on the development of instabilities and subsequent transition processes in hypersonic boundary layers (HBLs). A sequence of linear stability theory, nonlinear two-dimensional and three-dimensional direct numerical simulations is used to analyse Mach 6 boundary layers, with wall temperatures ranging from near-adiabatic to highly cooled conditions, where the second-mode instability is accompanied by radiation of energy. Decomposition of linear stability modes into their fluid-thermodynamic (acoustic, vortical and thermal) components shows that this radiation comprises both acoustic as well as vortical waves. Furthermore, in these cases, two-dimensional simulations show that the conventional 'trapped' nature of second-mode instability is ruptured. A quantitative analysis indicates that although the energy efflux of both acoustic and vortical components increases with wall cooling, the destabilization effect is much stronger and no significant abatement of pressure perturbations is realized. The direct impact of these mechanisms on the transition process itself is examined with high-fidelity simulations of three-dimensional second-mode wavepacket propagation. In the near-adiabatic HBL, the wavepacket remains trapped within the boundary layer and attenuates outside the region of linear instability. However, wavepackets in the cooled wall HBLs amplify and display nonlinear distortion, and transition more rapidly. The structure of the wavepacket also displays different behaviour; moderately cooled walls show bifurcation into a leading turbulent head region and a trailing harmonic region, while highly cooled wall cases display lower convection speeds and significant wavepacket elongation, with intermittent spurts of turbulence in the wake of the head region. This elongation effect is associated with a weakening of the lateral jet mechanism due to the breakdown of spanwise coherent structures. These features have a direct impact on wall loading, including skin friction and heat transfer. In moderately cooled walls, the spatially localized wall loading is similar to those in near-adiabatic walls, with dominant impact due to coherent structures in the leading turbulent head region. In highly cooled walls, the elongated near-wall streaks in the wake region of the wavepacket

† Email address for correspondence: usasidharannair@fsu.edu

result in more than twice as large levels of skin friction and heat transfer over a sustained period of time.

Key words: boundary layer stability, compressible boundary layers, transition to turbulence

1. Introduction

The problem of managing drag and heat transfer changes associated with transition to turbulence in hypersonic boundary layers is predicated on a detailed understanding of the relevant instability mechanisms. Hypersonic boundary layers (HBLs) harbour multiple instability modes, and display several possible routes to transition (Reshotko 1976). The broad range of parametric sensitivity of HBLs to perturbation evolution introduces significant challenges. In addition to factors such as free stream conditions and geometrical features, a key parameter governing instability growth in HBLs is the wall thermal condition. The most unstable Mack mode (or second-mode) instability in HBLs (Mack 1975, 1984) is particularly sensitive to the wall temperature. Cooling destabilizes this mode, making the HBL more susceptible to transition (Mack 1975; Stetson & Kimmel 1992). In addition, the origin of this unstable second mode shifts from the slow acoustic spectrum to the fast acoustic spectrum (Fedorov & Khokhlov 2001). Cold wall conditions are especially relevant when interpreting results from high-enthalpy experimental facilities, where the thermal inertia of test surfaces maintains wall temperatures much lower than the recovery temperature.

An important feature of the second mode in the context of cold walls is the identity and phase-speed variation of the most unstable mode. Under certain conditions this mode could travel at supersonic speeds with respect to the free stream in outer boundary layer regions, resulting in radiation of waves into the free stream, and oscillatory behaviour in the corresponding eigenfunction. For example, Chang, Vinh & Malik (1997) identify such supersonic modes in the presence of chemical equilibrium and non-equilibrium conditions in HBLs. Supersonic modes have also been confirmed through prior theoretical and numerical studies (Mack 1990; Bitter & Shepherd 2015; Chuvakhov & Fedorov 2016). Knisely & Zhong (2019*a*) provide detailed schematics and describe the wall-normal profiles in the non-radiating and radiating modes.

Recent efforts have also made progress on understanding changes in inter-modal dynamics as the wall is cooled. Knisely & Zhong (2019*b*) used direct numerical simulations (DNS) to identify resonant-type interactions between the slow and fast discrete modes with the slow continuous acoustic spectra. This highlights a complex set of dynamics contributing to the genesis of phenomena, such as the supersonic mode, that strongly motivate the augmentation of theoretical approaches with high-fidelity numerical simulations. Chang, Kline & Li (2019) studied the evolution of supersonic modes over an axisymmetric cone that resulted in non-acoustic radiation into the free stream, and associated it to the phase-speed synchronization between the instability and acoustic waves in non-parallel HBLs. A particularly interesting observation, with significant potential practical implication, emerges from the DNS of Chuvakhov & Fedorov (2016), who report that radiation by supersonic instability waves arising under cooled wall conditions redistributes energy from higher to lower frequencies. This may constitute a mechanism to mitigate instability growth, and eventually transition, in HBLs.

The generation of unstable modes with supersonic phase speeds is related to the influence of wall cooling on the mean-flow features. In general, cooling increases

gradients in the boundary layer, which can affect perturbation evolution past nonlinear saturation and alter the associated spatio-temporal scales. The enhanced gradients, along with baroclinicity, can also strengthen the generation of vorticity (Shadloo & Hadjadj 2017). Direct numerical simulations by Salemi & Fasel (2018) reveal that a prominent signature of linear instability mechanisms persists even in the nonlinear evolution phase of three-dimensional wavepackets on a wall-cooled hypersonic cone. Huang, Bretzke & Duan (2019) showed that even under turbulent conditions, wall cooling introduces more deviations from Boussinesq and Reynolds analogy assumptions. This resulted in erroneous predictions of Reynolds normal stresses and turbulent transverse heat fluxes, with implications for turbulence modelling of HBLs.

The present work builds on the above understanding of the effect of wall cooling on HBL transition by considering a spectrum of increasingly higher-fidelity techniques on a broad range of wall temperatures ranging from near-adiabatic to highly cooled conditions. The primary objectives may be succinctly stated as follows.

(i) Employ linear stability theory to characterize the changes to the second mode across the different wall temperatures, including changes in identity, phase-speed and fluid-thermodynamic content that ultimately yield acoustic radiation.
(ii) Use two-dimensional (2-D) DNS to document the changes in the 'trapped' nature (Fedorov 2011) of the second-mode instability with wall cooling, and to subsequently quantify the efflux of acoustic and vortical energy from the HBL due to supersonic mode radiation.
(iii) Assess, through three-dimensional (3-D) DNS, the impact of supersonic modes on the breakdown process, and identify the primary features of turbulence development in wall-cooled HBLs.

To place the results in the proper context in the available literature, the flow field studied corresponds to a free stream Mach number (M_∞) of 6 (Chuvakhov & Fedorov 2016), and wall to free stream temperature ratios ranging from 7 to 0.1 (§ 2).

The dynamics of HBL stability modes has been well established for the adiabatic (hot) wall case. Wave speed synchronization of different eigenmodes of the linear stability theory (LST) equations, has been associated with critical changes in the dynamics of prominent instabilities. For consistency, we adopt the convention in Fedorov & Tumin (2011), which identifies the two discrete instability modes relevant to HBLs as mode S and mode F. These discrete modes originate from the slow and fast acoustic wave speed limits, $(1 - 1/M_\infty)$ and $(1 + 1/M_\infty)$, respectively. The synchronization of mode F and the continuous vortical/entropic spectra is associated with enhanced sensitivity of this instability to free stream turbulence or hotspots (Fedorov & Tumin 2003). Mode F synchronization with mode S is followed by the latter becoming unstable for the second time (second mode) in adiabatic and warm walls (Ma & Zhong 2003). In sufficiently cooled walls however, mode F becomes unstable following this synchronization (Fedorov & Khokhlov 2001), and it eventually synchronizes with the slow continuous acoustic spectra. The previously noted supersonic radiating modes appear beyond this point.

In § 3 linear theory is first utilized to quantify these observations in the cold walls under consideration in this study. Key aspects, including changes in the identity of the most unstable mode (F or S) with wall cooling, are identified and the corresponding effects on the eigenfunctions are elaborated. In order to better understand the observed radiation in cooled wall layers, these stability modes are connected to their physical nature by decomposing their content into fluid-thermodynamic (FT) or Kovásznay-like components, using the procedures outlined in Doak (1989), Unnikrishnan & Gaitonde (2019*b*).

For reasons summarized in context below, the FT components, i.e. fluctuations having pure vortical, acoustic and thermal character, are extracted using $\rho \boldsymbol{u}$, where ρ is the density and $\boldsymbol{u}$ is the velocity vector. This procedure complements the mathematical insight obtained from LST and provides novel insights into the nature of waves radiated from the supersonic mode, such as whether, for example, the radiation is purely acoustic in nature (Salemi & Fasel 2018).

The influence of radiation on the initial receptivity and linear growth processes cannot be fully portrayed by the linear stability modes. A natural next step, discussed in § 4, is to examine the growth of linear harmonic perturbations in the 2-D boundary layer. Such simulations recreate the expected behaviour of the second-mode instability under various cold wall conditions. The splitting into FT components is repeated in this case; the feature that the split components of $\rho \boldsymbol{u}$ represent mass fluxes having direction accrues an immediate benefit that it can be used to examine how acoustic flux lines differ between non-radiating and radiating boundary layers. Specifically, the anticipated change from a compact trapped acoustic component at higher wall temperatures to a non-compact radiating one when the wall is cooled, is examined in detail.

The FT content, while insightful, does not directly inform the question of how radiating modes influence transition. One approach is to quantify such effects through the resulting energy efflux from the HBL. A highly effective way to quantify this energy loss is to examine the flux of the total fluctuating enthalpy (TFE), H', where H is the total enthalpy ($H = c_p T + \boldsymbol{u} \cdot \boldsymbol{u}/2$, with c_p and $\boldsymbol{u}$ being the specific heat at constant pressure and the velocity vector, respectively). The method has previously been successfully employed to examine the sources and sinks of near-wall acoustic energy in the second mode for adiabatic walls (Unnikrishnan & Gaitonde 2019*b*). In the present work, the technique is applied to the outer part of the boundary layer for each wall condition, to provide a uniform assessment of energy losses associated with boundary layer radiation. The discussion then assimilates the effect of radiation on transition dynamics, and the potential for transition mitigation.

A realistic understanding of the breakdown process following nonlinear saturation requires a fully 3-D analysis, which can yield crucial insights on changes in fundamental mechanisms across broad parameter ranges where transition sensitivity is observed. For example, using DNS, Jocksch & Kleiser (2008) observed streamwise elongated tails and slower convective speeds of turbulent spots in a moderately cooled Mach 5 boundary layer, compared with those in HBLs with a near-adiabatic wall temperature. At similar levels of cooling, Redford, Sandham & Roberts (2012) report spanwise coherent structures that extend into the calmed region behind the turbulent spot in a Mach 6 boundary layer. These structures are attributed to the destabilized second-mode instabilities that coexist with the turbulence in the spot. In § 5 3-D DNS are performed on a range of wall temperatures; the boundary layers are excited using wavepackets, whose features are informed by the linear theory and perturbation analyses discussed above. In addition to changes in the physical characteristics of the wavepacket structure as it propagates downstream at different wall temperatures, several pertinent trends are identified in the evolution of nonlinearities and breakdown mechanisms. The consequences on near-wall pressure signatures and wall loading are emphasized. A detailed spectral analysis of disturbance evolution is presented to further quantify variations in the spatio-temporal features of turbulence generation. The consequent considerations for transition-prediction model development (see e.g. Park & Lauchle 2009) are also summarized.

The flow field conditions employed, meshes and algorithmic details, and aspects of the basic state at different wall temperatures are discussed in § 2. The influence of wall cooling

on the eigenspectra obtained from the linear stability equations, and their decomposition into FT components are presented in § 3. Two-dimensional simulation results using LST results to inform initial and boundary conditions are probed in § 4 to understand the pathways by which the radiating phenomena are established, and to quantify the energy efflux associated with the supersonic mode. Finally, in § 5 features of 3-D wavepacket propagation under different wall thermal conditions are described, including focus on the establishment of skin friction and heat transfer.

2. Basic state features with wall cooling

A flat plate boundary layer subject to a range of wall thermal conditions is considered at a free stream Mach number, $M_\infty = 6$. To establish a reference with existing studies, the flow conditions are chosen to be similar to those described for a sharp-edged plate in Chuvakhov & Fedorov (2016). The Reynolds number based on free stream parameters, $Re = \rho^*_\infty U^*_\infty L^*/\mu^*_\infty$, is 1×10^6, where $(\cdot)^*$ indicates a dimensional quantity, ρ^*_∞, U^*_∞ and μ^*_∞ are the free stream density, velocity and dynamic viscosity, respectively, and L^* is a reference length scale. A perfect gas model is adopted, with Prandtl number, $Pr = 0.72$, and ratio of specific heats, $\gamma = 1.4$. The temperature dependence of viscosity is modelled using the Sutherland law,

$$\frac{\mu^*}{\mu^*_\infty} = \frac{T^*_\infty + Su^*}{T^* + Su^*}\left(\frac{T^*}{T^*_\infty}\right)^{3/2}, \tag{2.1}$$

where the free stream reference temperature $T^*_\infty = 300$ K and $Su^* = 110.4$ K. The Cartesian coordinates, (x, y, z), represent streamwise, wall-normal and spanwise directions, respectively, with $x = 0$ denoting the leading edge of the plate. Here (u, v, w) are the velocity components in the Cartesian coordinate system, and p, ρ and T denotes pressure, density and temperature, respectively. In the discussion below, an overbar, $\overline{(\cdot)}$, represents a time-averaged quantity, and a prime, $(\cdot)'$, denotes a perturbation component.

The impact of wall cooling on instability properties relevant to transition in the HBL is evaluated with LST, 2-D and 3-D DNS at eight wall to free stream temperature ratios, $T_W = T^*_W/T^*_\infty$, summarized in the computational matrix of table 1.

Here $T_W = 7$ corresponds to the near-adiabatic wall temperature for this free stream flow, while the other choices result in moderately (Bitter & Shepherd 2015) and highly (Wright & Zoby 1977; Chuvakhov & Fedorov 2016) cooled conditions discussed in the literature. The lowest values considered aide in identifying the most impactful trends in the evolution of stability and transition mechanisms.

The effect of wall cooling on the laminar basic state is summarized in figure 1 using similarity profiles obtained from the Levy–Lees similarity solution (Anderson 2000).The results are plotted at a representative streamwise location, $x = 2$, in the non-dimensional physical coordinate system. Figures 1(a) and 1(b) display the velocity and temperature profiles, respectively. Figure 1(c) shows the function $F1 = (\partial/\partial y)((1/T)(\partial u/\partial y))$ to identify generalized inflection points (GIPs) in the laminar flow, which are an indication of inviscid instability. As evident in figures 1(a) and 1(b), the hydrodynamic and thermal boundary layers progressively become thinner as the surface is cooled and the flow density increases. This leads to higher near-wall gradients and correspondingly higher wall loading. These trends are also manifested in the profiles of $F1$; specifically, the y-location of the peak value of the gradient appears closer to the wall with increased cooling. Prior to breakdown, both first- and second-mode instabilities usually exhibit maximum amplitudes

T_W	Analyses
7	1D-LST, 2D-DNS, 3D-DNS
5	1D-LST, 2D-DNS
3	1D-LST, 2D-DNS, 3D-DNS
1	1D-LST, 2D-DNS, 3D-DNS
0.7	1D-LST, 2D-DNS
0.5	1D-LST, 2D-DNS, 3D-DNS
0.3	1D-LST, 2D-DNS, 3D-DNS
0.1	1D-LST, 2D-DNS, 3D-DNS

Table 1. Cases studied with varying degree of wall cooling.

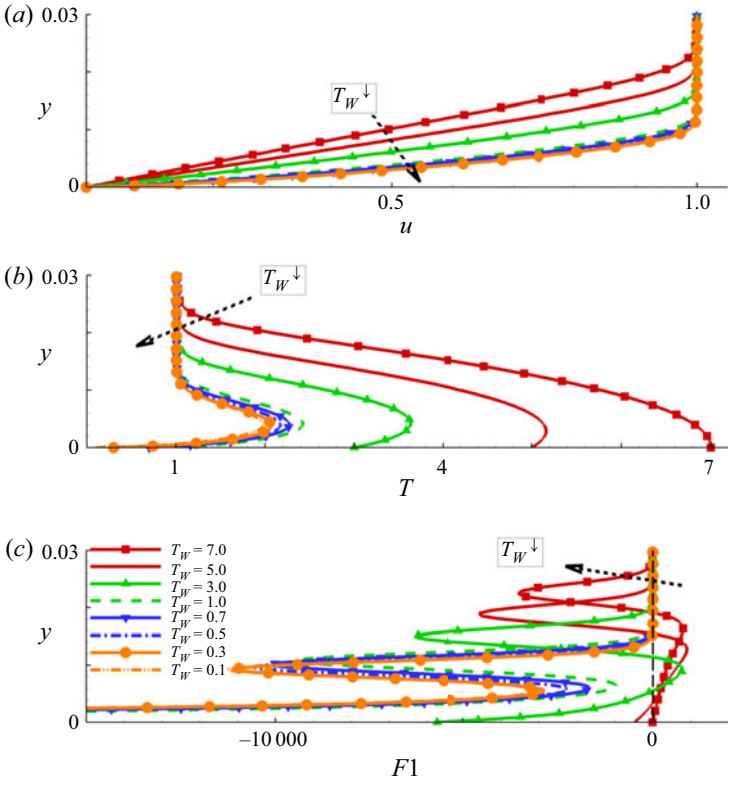

Figure 1. Effect of wall cooling shown using similarity profiles of (*a*) streamwise velocity, (*b*) temperature and (*c*) function, F1. The arrows indicate the trends in the profiles with decreasing values of wall temperature. The profiles are plotted at a streamwise location, $x = 2$. The vertical dashed line in (*c*) marks $F1 = 0$.

in the vicinity of this high-gradient region; thus, transition dynamics is enhanced nearer the wall for colder surface conditions.

Zero crossings of $F1$ indicate the existence of GIPs. For the near-adiabatic wall, $T_W = 7$, a single GIP is observed at $y \sim 0.02$. With moderate cooling, a second GIP appears in the inner boundary layer, as seen for $T_W = 5$ and $T_W = 3$. With further wall cooling, the upper and lower GIPs arise closer to each other, and eventually, effectively cancel each other. For the cases reported here, profiles for $T_W = 1$ and lower do not exhibit a GIP.

Zhang, Liu & Luo (2016) note that the absence of a GIP does not prevent the laminar profile from harbouring inviscid instabilities. For cold walls, a region could exist in the boundary layer where the absolute relative Mach number, $|M_R|$, of an instability wave is locally supersonic with respect to the mean flow. Here $M_R = (u - c)/a$, where c is the phase speed of the instability and a is the local speed of sound. Note that $|M_R| > 1$ corresponds to an inviscid instability of the Rayleigh equation (Lees & Lin 1946; Zhang *et al.* 2016); in this manner, highly cooled boundary layers can support second-mode instabilities.

3. Eigenspectra and their FT content

Laminar profile variations resulting from wall cooling profoundly affect linear instability mechanisms in boundary layers, as noted by several researchers (see, e.g. the discussion by Knisely & Zhong 2019*a*). Prior to evaluating its impact on transition pathways, it is instructive to characterize the key mechanisms using a simplified temporal stability analysis. For this, we first obtain the local eigenspectra for various wall temperatures to track the evolution of the relevant unstable mode, and subsequently analyse its FT composition.

3.1. *Linear stability results*

The linearized Navier–Stokes equations, under the assumption of a one-dimensional laminar basic state, is subjected to an eigenvalue analysis. The ansatz,

$$\phi = \bar{\phi} + \phi', \quad \phi' = \hat{\phi}(y)\, \mathrm{e}^{\mathrm{i}(\alpha x + \beta z - \omega t)}, \tag{3.1a,b}$$

is utilized, where ϕ is any primitive variable. Here $\overline{(\cdot)}$ and $(\cdot)'$ denote time-averaged and perturbation quantities, respectively; α and β are the (real) streamwise and spanwise wavenumbers, respectively; ω is the (complex) circular frequency. On the wall, the velocity and temperature perturbations are zero, due to no-slip and isothermal conditions, respectively.

The loci of unstable discrete modes are shown in figure 2 for the different wall temperature conditions.The horizontal and vertical axes are the real (speed, c_r) and imaginary (amplification rate, c_i) components of the phase speed of the instability wave. The horizontal dashed line marks the neutral limit while the vertical lines on the left, centre and right mark the wave speeds $(1 - 1/M_\infty)$, 1 and $(1 + 1/M_\infty)$, respectively, corresponding to the slow acoustic, entropic/vortical and fast acoustic waves in the free stream. These results are obtained for a wave with streamwise wavelength, $\lambda = 0.025$, at various streamwise locations in the range, $1 \leq x \leq 7$. For the near-adiabatic wall, $T_W = 7$, mode S (shown green in these figures) becomes unstable as seen in figure 2(*a*), resulting in second-mode instability. Mode F remains damped throughout this streamwise extent, and is thus not shown. This feature remains similar for moderate wall cooling, as seen for $T_W = 5$ and $T_W = 3$.

For the next case analysed, $T_W = 1$, mode S is stabilized, and second-mode instability now results from the positive growth rate of mode F (Fedorov & Khokhlov 2001), whose locus, shown in figure 2(*d*), is plotted in red. All lower wall temperature values, $T_W \leq 1$, show similar behaviours (figure 2*d–h*). Quantitative trends are clearly discernible: as the wall is progressively cooled, the instability of mode F extends to lower phase speeds, indicating that lower frequencies are appended into the unstable range. Figures 2(*f*)–2(*h*) further show that for the wave parameters considered, a near-neutral mode F interacts with

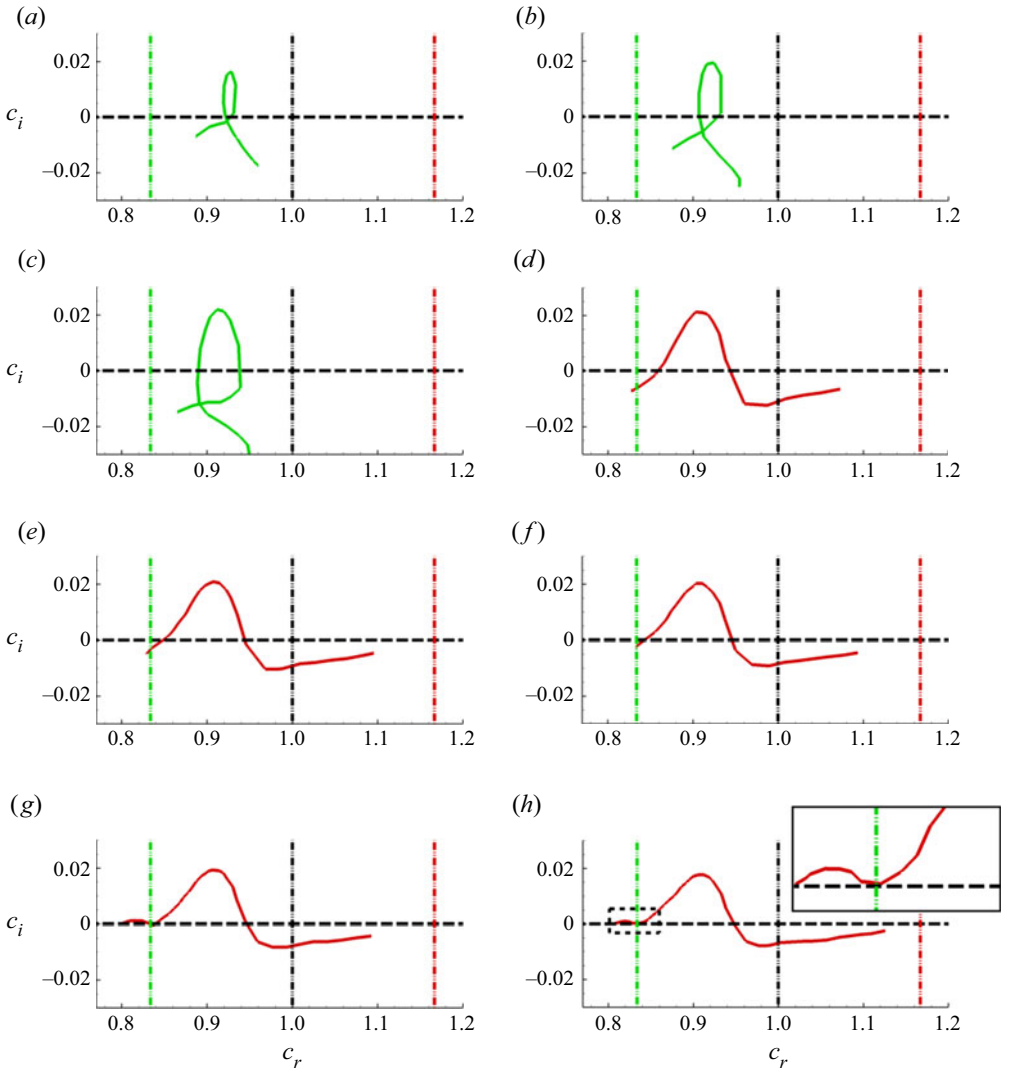

Figure 2. Loci of the unstable discrete mode obtained for the wave with $\lambda = 0.025$. Green and red loci have their origins near the slow and fast continuous acoustic spectra, respectively. The horizontal dashed lines mark $c_i = 0$. The vertical dashed–dotted lines on the left, centre and right mark the wave speeds, $(1 - 1/M_\infty)$, 1 and $(1 + 1/M_\infty)$, respectively. The inset in (h) magnifies the region marked within the dashed rectangle. (a) $T_W = 7$, (b) $T_W = 5$, (c) $T_W = 3$, (d) $T_W = 1$, (e) $T_W = 0.7$, (f) $T_W = 0.5$, (g) $T_W = 0.3$, (h) $T_W = 0.1$.

the slow continuous acoustic spectrum. More interestingly, for $T_W = 0.3$ and $T_W = 0.1$, a second zone of instability is present in the domain $c_r < (1 - 1/M_\infty)$, following a 'kink' near this speed limit, consistent with the results of Bitter & Shepherd (2015). This region of mode F instability is highlighted in figure 2(h) using an inset. The presence of a weakly damped or unstable mode F at phase speeds lower than $(1 - 1/M_\infty)$ has been observed to result in radiation into the free stream. For the cases reported here, this phenomena exists in scenarios where $T_W \leq 1$.

To identify relevant frequencies and neutral limits associated with the instability waves, we summarize the eigenspectra and amplification rates for the two extreme cases studied

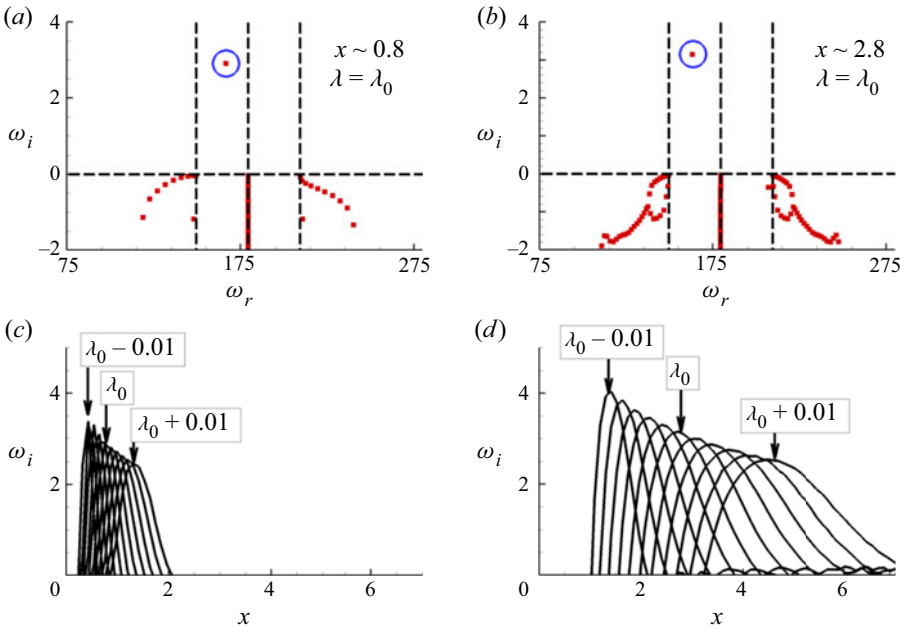

Figure 3. Eigenspectrum in the vicinity of the peak amplification of the second mode for (*a*) $T_W = 7$ and (*b*) $T_W = 0.1$. The horizontal dashed lines mark $\omega_i = 0$. The vertical dashed lines on the left, centre and right mark the circular frequencies corresponding to the wave speeds, $(1 - 1/M_\infty)$, 1 and $(1 + 1/M_\infty)$, respectively. Variation in the amplification rate as the instability wavelength is varied uniformly in the range, $\lambda_0 - 0.01 \leq \lambda \leq \lambda_0 + 0.01$, for (*c*) $T_W = 7$ and (*d*) $T_W = 0.1$, in increments of 0.002.

here ($T_W = 7$ and $T_W = 0.1$) in figure 3. Figures 3(*a*) and 3(*b*) plot the eigenspectrum in terms of circular frequency, (ω_r, ω_i), in the vicinity of the peak amplification of the second mode for $T_W = 7$ and $T_W = 0.1$, respectively. The unstable mode in each case is marked by a circle, and the wavelength chosen ($\lambda_0 = 0.025$) corresponds to that used to obtain the loci in figure 2. Figures 3(*c*) and 3(*d*) show the variation in the neutral limit of the instability identified above, when λ is varied uniformly in the range, $\lambda_0 - 0.01 \leq \lambda \leq \lambda_0 + 0.01$, for $T_W = 7$ and $T_W = 0.1$, respectively. In both cases, the streamwise region of instability increases for larger wavelengths, although the peak amplification rate decreases. For any given wave, the cooler wall exhibits a longer region of instability at a relatively downstream location. The supersonic region of instability is evident in the cooler wall, particularly at higher wavelengths.

The behaviour of the unstable eigenmode is qualitatively different prior to and after the synchronization of mode F phase speed with $1 - 1/M_\infty$. This is demonstrated in figure 4, which plots the pressure eigenfunctions at two locations, $x = 4.3$ (before synchronization) and $x = 5$ (after synchronization), for $T_W = 0.1$ in figures 4(*a*) and 4(*b*), respectively.Prior to the synchronization, the eigenfunction has the typical compact form with a single zero crossing associated with the second-mode instability (Mack 1984). Once the phase speed of the instability wave falls below $(1 - 1/M_\infty)$, the outer region exhibits an oscillatory behaviour. The phase-speed relations at these two locations are further examined in figures 4(*c*) and 4(*d*). Profiles of mean velocity (u), fast acoustic ($u + a$) and slow acoustic ($u - a$) speeds, and the relative Mach number ($M_R = (u - c)/a$) are plotted together with the phase speed of the instability wave, c_r, represented by a vertical dashed–dotted line. The profiles show that at $x = 4.3$, $M_R < 1$ at all wall-normal locations. Since the wave is

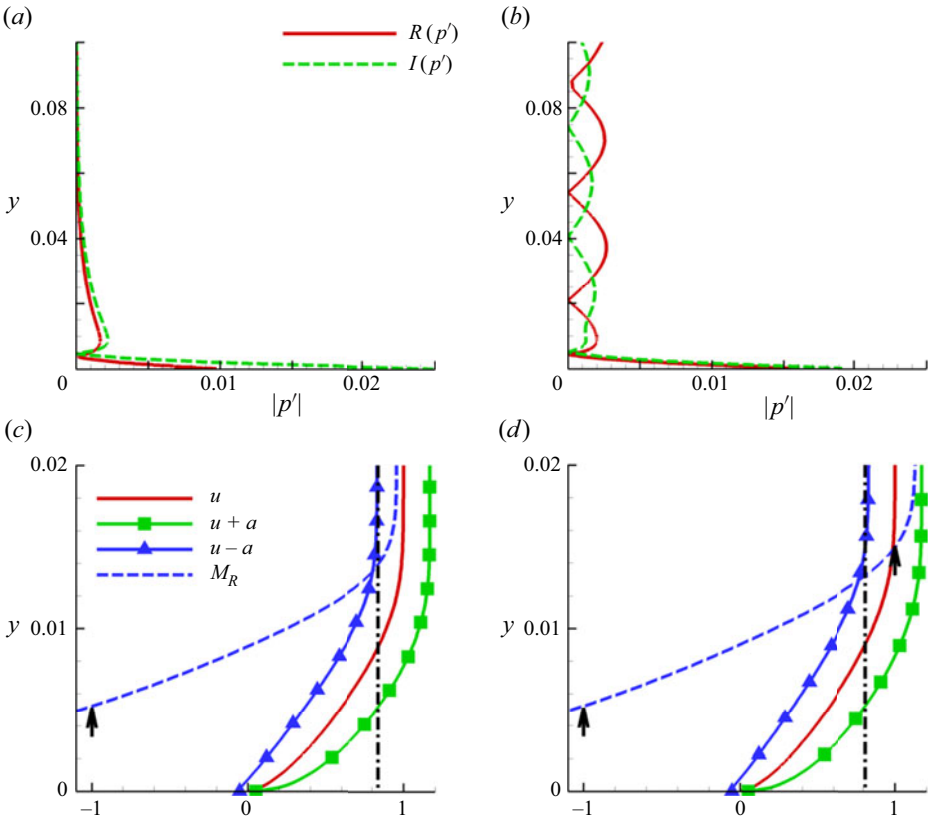

Figure 4. Absolute values of real and imaginary components of the pressure eigenfunction, $R(p')$, and $I(p')$, respectively, plotted at (*a*) $x = 4.3$ – prior to synchronization and (*b*) $x = 5$ – after synchronization. Profiles of various speed limits as indicated, plotted at (*c*) $x = 4.3$ and (*d*) $x = 5$. The vertical dashed–dotted lines in (*c*) and (*d*) mark the phase speed of the corresponding unstable wave.

then subsonic relative to the mean flow in the outer boundary layer, it decays into the free stream. However, it is supersonic relative to the mean flow near the wall ($M_R < -1$), in the region, $0 \leq y \leq 0.0052$; this location is marked by the vertical arrow which indicates the sonic limit, $M_R = -1$. At $x = 5$, the lower supersonic region remains similar to that observed prior to synchronization. The eigenfunctions below this sonic limit also appear similar in figures 4(*a*) and 4(*b*). However, M_R now exceeds the sonic limit in the outer boundary layer as well, which is also marked by a second vertical arrow at $y \sim 0.015$ (figure 4*d*), where $M_R = 1$. This relative supersonic region results in wave radiation into the free stream, consistent with the oscillatory eigenfunction.

3.2. *Physical nature of eigenmodes*

The above eigenspectrum analysis provides a mathematical description of the behaviour of instabilities. In such scenarios, where the qualitative behaviour of instabilities varies in a meaningful fashion, a physics-based interpretation can provide complementary insights into key flow mechanisms (Tumin 2020*a*). For this, we adopt a Kovásznay-type framework, which decomposes fluctuations in terms of three physical components: vortical, acoustic and entropic, referred to earlier as FT components. This framework

is used to study the composition of instabilities in the vicinity of synchronization; this facilitates a better understanding of the physical changes induced in mode F due to wall cooling. The momentum potential theory of Doak (1989) provides an effective way to achieve the desired splitting without linearization. Specifically, it can be shown that the 'momentum-density' vector, $\rho\boldsymbol{u}$, can be split precisely into rotational and irrotational mean and fluctuating components. The former represents the vortical component while the latter can be (again exactly) further decomposed into acoustic (irrotational and isentropic) and entropic (irrotational and isobaric) components. Details of the procedure, and implementation for LST as well as DNS data, may be found in Unnikrishnan & Gaitonde (2016, 2018) for free shear layers and Unnikrishnan & Gaitonde (2019*b*) for wall-bounded layers. Briefly, the decomposition can be expressed as

$$\rho\boldsymbol{u} = \bar{\boldsymbol{B}} + \boldsymbol{B}' - \boldsymbol{\nabla}\psi', \quad \boldsymbol{\nabla}\cdot\bar{\boldsymbol{B}} = 0, \quad \boldsymbol{\nabla}\cdot\boldsymbol{B}' = 0, \tag{3.2a–c}$$

where $\bar{\boldsymbol{B}}$ and $\boldsymbol{B}'$ are the mean and fluctuating parts of the vortical component, respectively. The irrotational component, $-\boldsymbol{\nabla}\psi'$, may be further split to obtain the acoustic ($-\boldsymbol{\nabla}\psi'_A$) and vortical ($-\boldsymbol{\nabla}\psi'_T$) components through the following Poisson equations (Unnikrishnan & Gaitonde 2019*b*):

$$\nabla^2\psi' = \frac{\partial\rho'}{\partial t}, \quad \nabla^2\psi'_A = \frac{1}{a^2}\frac{\partial p'}{\partial t}. \tag{3.3a,b}$$

$$\psi' = \psi'_A + \psi'_T. \tag{3.4}$$

Here t is time and a is the local sonic speed. For convenience, we adopt the following notation for the FT variables in 2-D space: $\boldsymbol{B}' = (B'_x, B'_y)$, $-\boldsymbol{\nabla}\psi'_A = \boldsymbol{A}' = (A'_x, A'_y)$ and $-\boldsymbol{\nabla}\psi'_T = \boldsymbol{\tau}' = (\tau'_x, \tau'_y)$.

The decomposition of cold wall eigenfunctions shows very different behaviour from those of the adiabatic wall previously described in Unnikrishnan & Gaitonde (2019*b*). The extracted FT components of the eigenfunctions of the coldest wall, $T_W = 0.1$, are analysed prior to and after synchronization in figure 5, using the modulus of the streamwise and wall-normal components. The streamwise locations correspond to those in figure 4. The top, middle and bottom rows correspond to the vortical, acoustic and entropic components, respectively. The left and right columns display the FT decomposition of the eigenfunctions before and after the synchronization. The FT composition prior to synchronization indicates that the vortical component is the dominant one in the Mack mode instability over highly cooled walls, followed by the acoustic and entropic components. This hierarchy is consistent with corresponding results for an adiabatic wall (Unnikrishnan & Gaitonde 2019*b*). During post-synchronization however, the oscillatory eigenfunction exhibits an acoustic component in the free stream, as seen in figure 5(*d*) – this represents the observed acoustic radiation. Somewhat surprisingly, and confirmed later with DNS results, the FT decomposition also reveals that the radiated waves in the free stream contain a significant amount of vorticity, as seen in figure 5(*b*). Streamwise vortical fluctuations are considerably higher than the wall-normal component, and this difference amplifies in the downstream direction, as the wavefronts become increasingly inclined towards the wall. The contribution from the entropic component to free stream radiation remains negligible. Thus, the emission from cold HBLs resulting from supersonic phase speeds of instabilities contains comparable amounts of vortical and acoustic waves that propagate in the free stream. Having characterized the linear mechanisms, we next quantify the perturbation growth and energy efflux in these HBLs, by adopting a high-fidelity numerical approach.

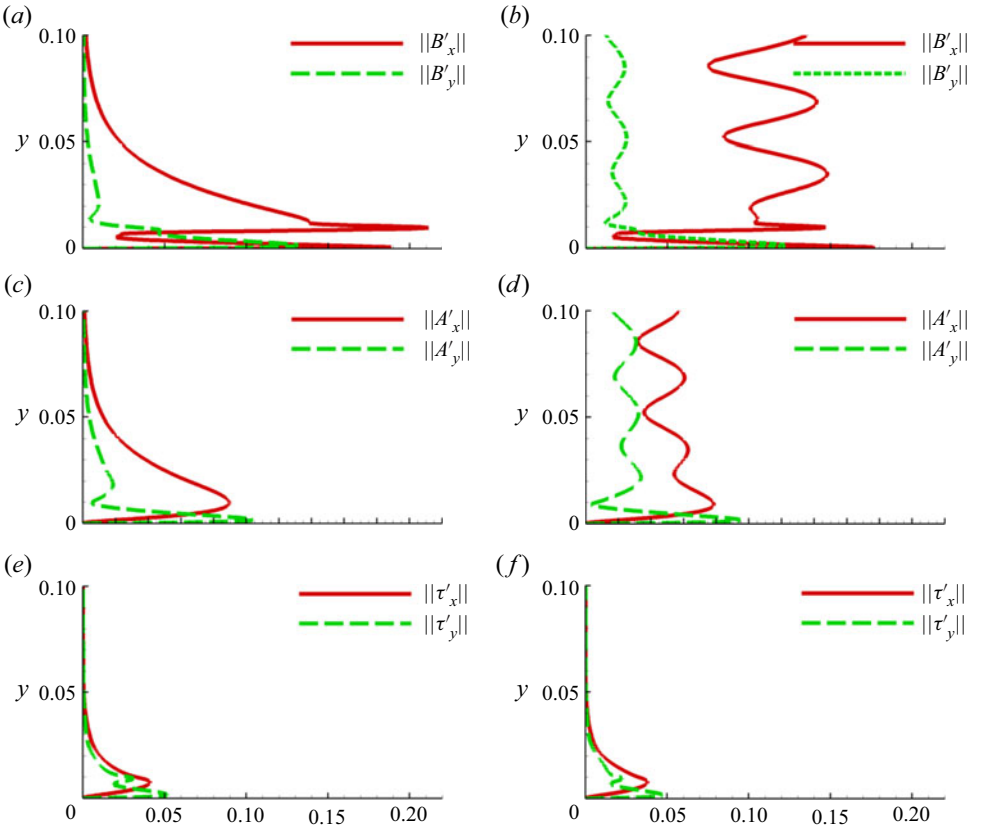

Figure 5. Modulus of streamwise and wall-normal components of (*a*) vortical, (*c*) acoustic and (*e*) entropic constituents of the unstable eigenmode at $x = 4.3$. Plots (*b*), (*d*) and (*f*) show the corresponding results at $x = 5$.

4. Analyses of linear perturbations with 2-D DNS

The above results show that wall cooling can introduce significant variations in perturbation growth characteristics of HBLs. In this section the relative behaviour of the different cold wall HBLs is examined for all cases listed in table 1, by adopting DNS to capture the spatio-temporal evolution of second-mode instabilities.

4.1. *Laminar and forced DNS*

The simulations solve the 2-D, unsteady Navier–Stokes equations in curvilinear coordinates. To ensure sufficient resolution, a seventh-order weighted essentially non-oscillatory (Balsara & Shu 2000) scheme is employed to reconstruct the characteristic variables. The inviscid fluxes are then obtained using the Roe scheme (Roe 1981), along with an entropy fix (Egorov, Fedorov & Soudakov 2006). Fourth-order central differences are used to discretize the viscous terms. Time integration is performed using a nonlinearly stable third-order Runge–Kutta scheme (Shu & Osher 1988). To improve the robustness of the solver, the high-order reconstruction is substituted by a third-order upwind scheme in the vicinity of shocks (Bhagatwala & Lele 2009), along with the van-Leer harmonic limiter (van Leer 1979), to minimize grid-scale oscillations.

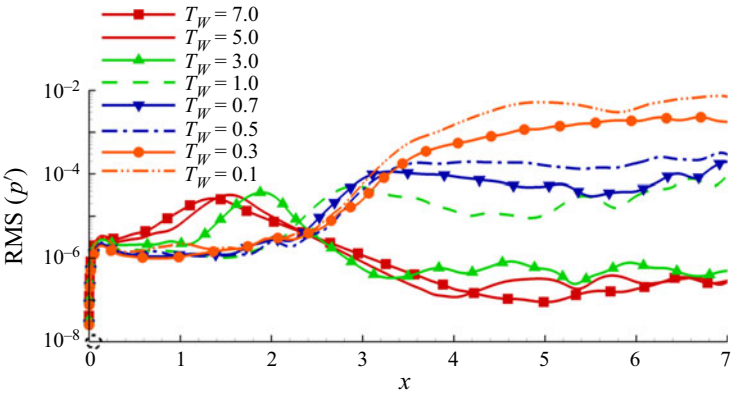

Figure 6. Streamwise variation of RMS values of wall-pressure perturbations for various cold walls. The dashed circle on the horizontal axis marks the streamwise location of the actuator.

The computational domain spans $0 \leq x \leq 7$ and $0 \leq y \leq 1.32$, thus including the leading edge of the plate ($x = 0$) in the calculations. Supersonic inflow and outflow conditions are imposed on the upstream and downstream boundaries, respectively. Zero-normal-gradients are imposed on the free stream boundary. Wall cooling is simulated using isothermal conditions on the surface, as defined by T_W. For each case, the basic state is first obtained and, subsequently, perturbations are introduced in the form of harmonic wall-normal momentum perturbations to emulate a wall blowing-suction actuator (Egorov *et al.* 2006; Soudakov *et al.* 2016). The actuation in this set of forced DNS has the form

$$q_w(x, t) = \rho_w v_w = A_{2D} \sin\left(2\pi \frac{x - x_1}{x_2 - x_1}\right) \sin(\omega_{2D} t). \tag{4.1}$$

Here, q_w is the wall-normal momentum, A_{2D} is the forcing amplitude, and x_1 and x_2 define the streamwise extent of the actuator, $x_1 \leq x \leq x_2$. For all wall temperatures, the actuator is placed at $0.050 \leq x \leq 0.075$, to ensure that it is upstream of the region of second-mode instability. The linear stability analyses of § 3.1 reveal that in the chosen streamwise extent of the computational domain, a wave with circular frequency $\omega \sim 150$ exhibits linear amplification due to second-mode instability in all cases. Hence, this frequency is chosen to perturb all the mean flows ($\omega_{2D} = 150$). The forcing amplitude is chosen as $A_{2D} = 1 \times 10^{-4}$ to introduce perturbations in the linear range.

Cooling destabilizes the second mode, and the resulting higher growth rates increase the susceptibility of the HBLs to transition (Stetson *et al.* 1989; Stetson & Kimmel 1992). Wall-pressure perturbations provide a means to quantify this trend in the HBLs examined. The streamwise variation of wall-pressure perturbations is presented in terms of root-mean-square (RMS) values in figure 6 for all eight cases.The streamwise location of the actuator is also marked on the horizontal axis with a dashed circle. As expected, the warmer walls experience relatively weak amplification of perturbations. The peak values achieved increase with wall cooling, consistent with the destabilization of the Mack mode. The region of amplification also progressively shifts downstream, due to the thinning of the boundary layer in cooler HBLs. The peak amplitudes vary by over three orders of magnitude across the cases. For the warmer walls, the RMS perturbations attenuate outside the upper branch of the neutral curve. For highly cooled walls (typically $T_W \leq 1$), this attenuation is weak, and the high amplitudes are sustained over a prolonged region downstream. This could be the result of the merging of the weakly damped discrete mode

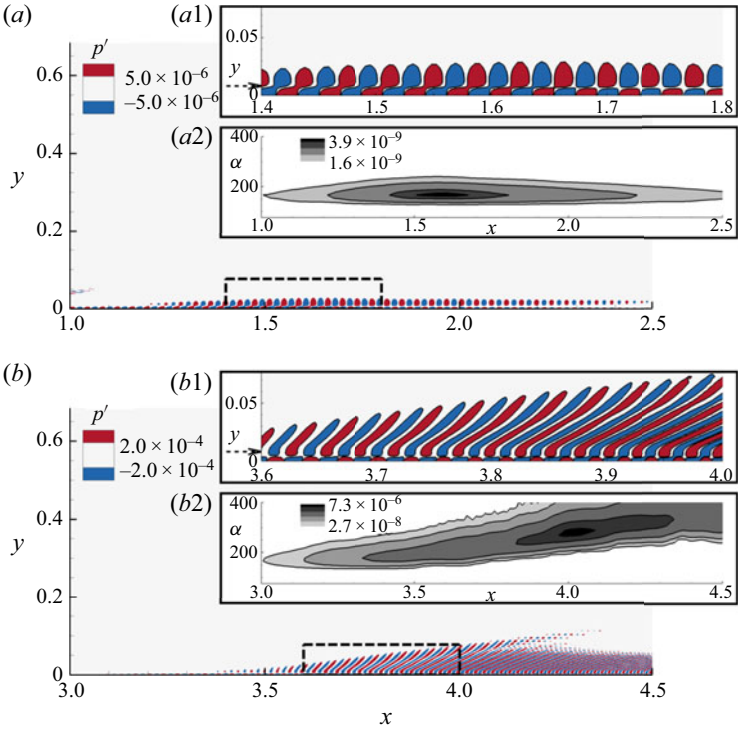

Figure 7. Pressure perturbation contours highlighting the form of the second-mode instability for (*a*) $T_W = 5$ and (*b*) $T_W = 0.1$. The regions marked by the dashed rectangles in (*a*) and (*b*) are magnified in the respective insets, (*a*1) and (*b*1). Insets (*a*2) and (*b*2) plot the space-wavenumber, x–α, variation in the pressure perturbation signal for $T_W = 5$ and $T_W = 0.1$, respectively, at a wall-normal location, $y \sim 0.008$. For reference, this location is marked with horizontal dashed arrows near the y-axes of insets (*a*1) and (*b*1).

with the continuous slow acoustic spectrum, resulting in inter-modal interactions, and is consistent with the observations in Chuvakhov & Fedorov (2016).

Key features of pressure perturbations in the second-mode instability in these HBLs are summarized in figure 7 using the pressure perturbation fields for $T_W = 5$ (figure 7*a*) and $T_W = 0.1$ (figure 7*b*). For each case, the region of second-mode amplification is displayed, and magnified views of the waveforms are provided in the respective insets (*a*1) and (*b*1). The warmer plate shows the classic second-mode lobes with a zero crossing near the GIP, and a compact wall-normal profile. For the cold wall however, these waves extend into the free stream at an acute angle relative to the plate. This angle decreases in the downstream direction, causing the wavefronts to align increasingly towards the wall.

This behaviour is consistent with the reduction of the phase speed of the instability, which is now more supersonic with respect to the free stream; as such, the waves propagate further out into the far field. Since the mechanism is linear, an accompanying continual increase in the wavenumber of the instability wave is observed. This is quantified with scalograms provided in the second inset of each panel of figure 7, (*a*2) and (*b*2), which track the variation in streamwise wavenumber, $\alpha = 2\pi/\lambda$, with x, at a wall-normal location, $y \sim 0.008$, marked for reference by a horizontal dotted arrow on the vertical axes in insets (*a*1) and (*b*1). Over the warmer wall, the instability wave maintains a near-constant wavenumber throughout the unstable region. The situation is clearly very different over the cooler wall, where the wavenumber increases as the wave amplifies in the HBL.

4.2. *Radiating modes and efflux of energy*

The efflux of energy from radiating HBLs may have the potential to materially impact the growth rates of perturbations, which in turn may present options to aid transition mitigation (Chuvakhov & Fedorov 2016). Fluid-thermodynamic dynamics is now employed to examine this physics in the region of instability growth captured in the DNS. The procedure followed is to first identify the physical mechanisms being affected due to wall cooling, and to then utilize this knowledge to quantify the energy radiated from the HBL.

Mack mode instabilities relevant to this study are essentially inviscid instabilities, that are generally accepted to exhibit a waveguide (or trapped) behaviour (Fedorov 2011) under adiabatic wall conditions, imparting them an acoustic character. A clearer understanding of how the properties of the trapped component changes when the wall is cooled, and the boundary layer starts radiating, aides the subsequent energy efflux study. Prior FT analysis of Mack modes in HBLs with adiabatic walls ($T_w \sim 7$) (Unnikrishnan & Gaitonde 2019*b*) has revealed that both mode F and mode S instabilities are composed of all three FT components (vortical, acoustic and entropic). However, the above waveguide behaviour is most clearly manifested in the acoustic component, i.e. flux lines associated with $\boldsymbol{A}'$ display alternating monopoles along an essentially horizontal line at approximately the height of the critical layer (where $u = c$). The warmer walls show the same behaviour; an example is shown by plotting aspects of the acoustic component for $T_W = 5$ in figure 8(*a*). The streamwise extent is chosen to represent a detailed view of the corresponding cases described previously in figure 7. The background contours represent the magnitude of the acoustic component, $\|\boldsymbol{A}'\|$. The arrow heads mark the direction of the flux lines which constitute the acoustic component of momentum fluctuations, (A'_x, A'_y), in the Mack mode. Note that since the decomposed variable is $\rho\boldsymbol{u}$, these effectively represent mass fluxes associated with the acoustic component. For the moderately cooled wall, $T_W = 5$, the acoustic flux lines are generally similar to those in the adiabatic case, with a zero-flux line existing at $y \sim 0.02$, corresponding to the critical layer of this instability wave. Clearly, this component is effectively trapped between the wall and the critical layer, since no flux lines cross the line joining the monopoles.

The same results for the highly cooled wall, $T_W = 0.1$, are shown in figure 8(*b*). Clearly, no zero-flux line exists here, and the arrows indicate that the supersonic mode displays flux transport between the HBL and the free stream due to the acoustic component. This is a manifestation of the acoustic part of the radiation associated with the supersonic mode. Since the vortical ($\boldsymbol{B}'$) and acoustic ($\boldsymbol{A}'$) fluctuations educed from DNS are inherently components of the momentum vector, they can transport energy in the flow field. These energy considerations, and a budget equation for transport of TFE by the different FT components, have been extensively detailed for the adiabatic HBL in Unnikrishnan & Gaitonde (2019*b*) and for high-speed jets in Unnikrishnan & Gaitonde (2016).

A quantification of the efflux of fluctuating energy associated with each FT component from the HBL requires a splitting of the TFE into those components. Such a splitting has been provided by Jenvey (1989). Since the cold walls considered in this work display radiating modes containing vorticity and acoustic waves in the free stream (see figures 5*b* and 5*d*), both fluxes of the respective energies are of principal importance here. Specifically, the transported energy variables that must be accounted for are H'_B and H'_A, which are the vortical and acoustic components, respectively, of H' and are defined as

$$H = c_p T + \boldsymbol{u}\cdot\boldsymbol{u}/2, \quad H = \bar{H} + H', \tag{4.2a}$$

$$H'_B = \left(\frac{\bar{c}}{\bar{\rho}}\right)\bar{\boldsymbol{M}}\cdot\boldsymbol{B}', \tag{4.2b}$$

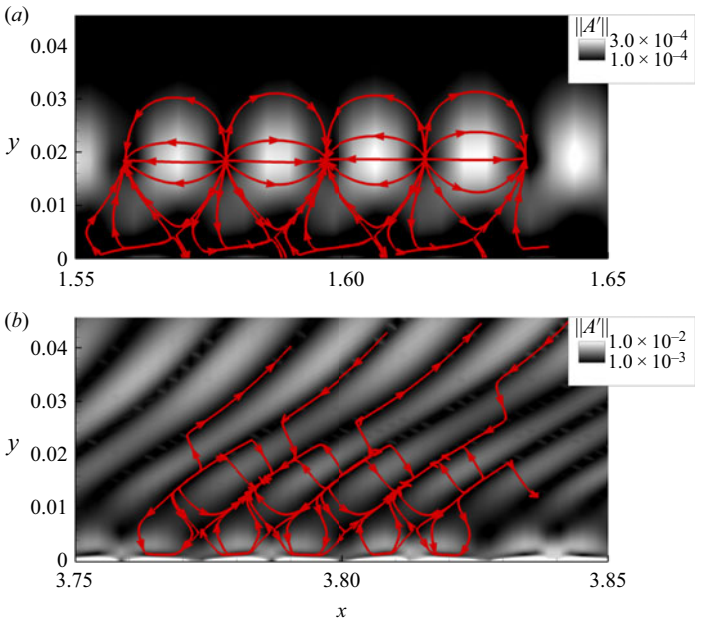

Figure 8. Flux lines of the acoustic component, (A'_x, A'_y), for (a) $T_W = 5$ and (b) $T_W = 0.1$. The contours represent the magnitude of the acoustic field.

$$H'_A = \left(\frac{p'}{\bar{\rho}}\right)(1 - \bar{\boldsymbol{M}} \cdot \bar{\boldsymbol{M}}) - \left(\frac{\bar{c}}{\bar{\rho}}\right)\bar{\boldsymbol{M}} \cdot \nabla \psi'_A, \tag{4.2c}$$

where $\boldsymbol{M} \equiv \boldsymbol{u}/c$ is the Mach number vector. The vortical flux of TFE in the wall-normal direction is calculated as $F_B = H'_B \boldsymbol{B}' \cdot \hat{j}$ and, similarly, the acoustic flux is $F_A = H'_A \boldsymbol{A}' \cdot \hat{j}$, where $\hat{j}$ is the unit normal in the wall-normal direction.

Accurate quantitative comparisons of perturbation energy fluxes require care in establishing consistency across all eight boundary layers examined. Indeed, use of the DNS described above for this purpose may be misleading, since the actuators are placed at the same streamwise location, but the neutral curves depend on the wall temperature. To ensure that the linear amplification is initiated at similar perturbation energy levels in each case, a second set of forced DNS is performed for all cases, with actuators placed at similar locations relative to the lower branch of the respective neutral curve. These locations can be identified for each mean flow using growth rates calculated from the amplitude of wall-pressure perturbations obtained from the first set of forced DNS discussed above. To minimize numerical noise contamination, the neutral curve is assumed to begin at the threshold, $\sigma = \mathrm{d}\{\ln[a_p(x)]\}/\mathrm{d}x \sim 2$ (Egorov *et al.* 2006), where σ is the numerical growth rate and $a_p(x)$ is the wall-pressure amplitude. Thus, for this second set of forced DNS, the streamwise extent of the actuator is defined as $x_1 = x_0$ and $x_2 = x_1 + 0.025$, where x_0 is the lower neutral limit of the respective HBLs. All other actuator parameters in (4.1) are identical to the first set of forced DNS. To prevent superfluous computations, the domain upstream of the neutral point is neglected by imposing corresponding laminar profiles at the inlet boundary. The outflow boundaries are placed approximately four non-dimensional length units downstream to ensure that the linear instability range is accommodated. The perturbation evolution and energy fluxes are analysed over this streamwise distance.

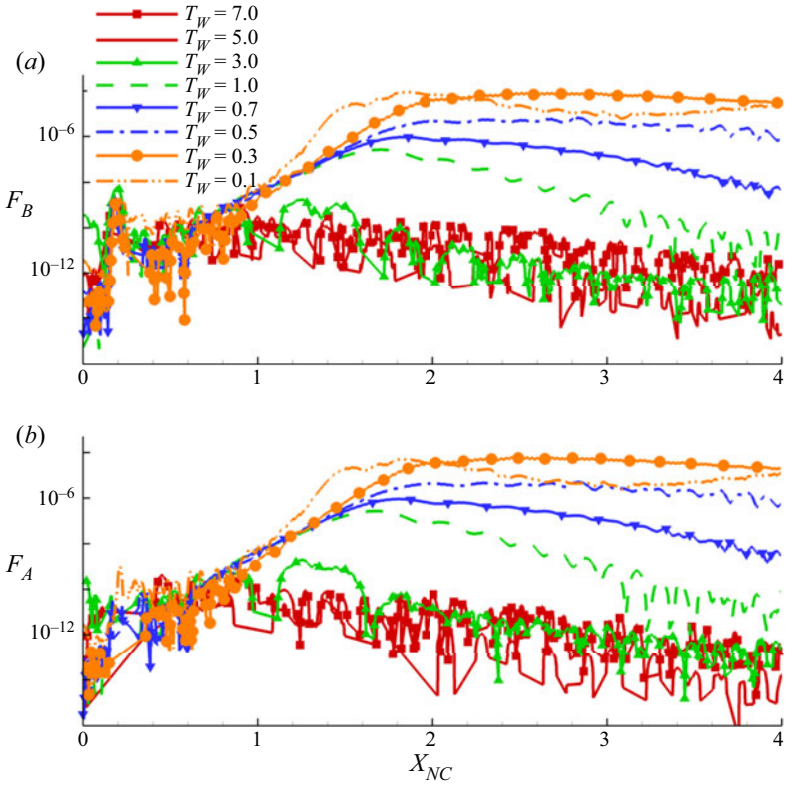

Figure 9. Streamwise variation of (*a*) vortical and (*b*) acoustic efflux of energy from the HBLs, for various cold walls. The actuator is placed at the lower neutral limit.

The hydrodynamic and acoustic energy fluxes, F_B and F_A, thus obtained are plotted in figure 9. Note that the streamwise direction is now represented using the displaced coordinate, $x_{NC} = x - (x_0 + \Delta x)$, with origin near the lower neutral limit. Here $\Delta x = 0.2$ is a small upstream displacement of the inlet boundary from this neutral limit, which is included to prevent the actuator from interfering with the inflow boundary conditions. For all cases, the fluxes are calculated at a surface located at $y \sim 0.04$, which is sufficiently outside the boundary layer. The positive values of fluxes indicate that F_A and F_B both constitute a net outflow of energy from each HBL. More interestingly, both these fluxes are of comparable magnitudes for a given wall temperature. This reinforces the observation made in the context of LST above, that vortical and acoustic mechanisms are equally significant in radiation processes from cooled HBLs. The radiative loss of energy is negligible for near-adiabatic and moderately cooled walls. The energy loss increases monotonically with wall cooling; in fact, when $T_W \leq 1$, the energy efflux is between five to six orders of magnitude higher than for moderately cooled wall boundary layers. The radiation from these highly cooled wall layers exhibits peak values slightly downstream of the location where the amplitudes of the linear waves achieve their maximum values on the surface. This is due to the forward inclination of the supersonic waves in the free stream, as observed earlier in figure 7(*b*).

The efflux of vortical and acoustic enthalpy diverts a portion of fluctuating energy from the primary second-mode instability mechanism. To evaluate the implication of the efflux on transition, the RMS of wall-pressure perturbations is shown in figure 10 for this second

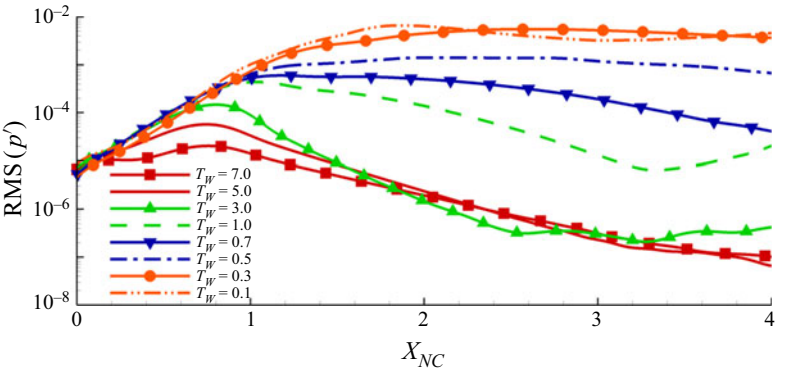

Figure 10. Streamwise variation of RMS values of wall-pressure perturbations for various cold walls, with the actuator placed at the lower neutral limit.

set of forced DNS. A main observation emerging from the figure is that the increases in radiative losses do not have a prominent impact on wall-pressure perturbations, whose value at any given distance increases monotonically with wall cooling. This indicates that the efflux due to the supersonic radiating mode is a higher-order effect and may not be sufficient to compensate for the first-order destabilizing effect of wall cooling on the second mode. This observation is not inconsistent with recent theoretical analysis by Tumin (2020*b*), who notes that the radiating component is limited to the 'tail' portion of second-mode wavepackets in cooled HBLs, and do not attenuate the primary amplification mechanism associated with the subsonic component.

5. Three-dimensional transition mechanisms in cooled HBLs

The above analysis addressed the fundamental aspects of stability modes and linear growth through LST and 2-D DNS. The problem of breakdown associated with transition requires a 3-D analysis; such an exercise is now conducted with fully 3-D DNS to describe the effects of radiating modes on transition in wall-cooled HBLs. Specifically, the evolution of spatio-temporally localized wavepackets is examined for representative cases as noted in table 1. Below, the numerical framework is first summarized, followed by a comprehensive qualitative and quantitative spectral and statistical description of the associated dynamics, including effects on wall loading.

5.1. *General features of 3-D response to wavepacket forcing*

The 3-D Navier–Stokes equations are solved using the high-order spatial schemes summarized in § 4.1. To facilitate feasible time-step sizes, the second-order diagonalized (Pulliam & Chaussee 1981) implicit Beam–Warming scheme is utilized for time integration (Beam & Warming 1978). The extent of the computational domain for each HBL in the 3-D DNS is as follows:

$$x_0 - \Delta x \leq x \leq x_0 - \Delta x + 4.1, \tag{5.1a}$$

$$0 \leq y \leq 0.43, \tag{5.1b}$$

$$-0.15 \leq z \leq 0.15. \tag{5.1c}$$

As discussed in the context of the second set of forced 2-D DNS employed for energy efflux considerations, x_0 is the lower neutral limit of the respective HBL, and $\Delta x = 0.2$. This design of the domain also ensures that the local boundary layer thickness for each HBL scales suitably to harbour the second mode instability induced by the chosen forcing parameters. The computational domain is composed of 4001, 261 and 151 nodes in the streamwise, wall-normal and spanwise directions, respectively, for all the wall temperatures reported here. Around 45 % of the points are clustered within the boundary layer height of the coldest wall, $T_W = 0.1$. A relatively finer wall spacing of $\Delta y_W = 8 \times 10^{-5}$ is utilized to ensure sufficient resolution of the cooler boundary layers, based on prior considerations for near-adiabatic wall temperatures (Unnikrishnan & Gaitonde 2019*a*). The boundary conditions are similar to those used in the 2-D simulations at the inflow, outflow, wall and far field boundaries, and the spanwise direction is assumed to be periodic. The time-step size adopted for the 3-D simulations is sufficient to resolve frequencies upto four times the spectral range activated by the wavepackets, as confirmed by the following analyses. Adequacy of the above grid parameters, and time-step size, is demonstrated through a grid study in the appendix. Three-dimensional wavepackets are introduced through wall blowing-suction, using the following actuator model (Novikov, Egorov & Fedorov 2016; Novikov 2017):

$$q_w(x, z, t) = \rho_w v_w = A_{3D}\ \sin\left(2\pi \frac{x - x_1}{x_2 - x_1}\right) \sin\left(\pi \frac{z - z_1}{z_2 - z_1}\right) \sin(\omega_{3D} t). \tag{5.2}$$

The forcing amplitude of the 3-D wavepacket, $A_{3D} = 5 \times 10^{-2}$, and the streamwise extent of the actuator is set to $x_1 = x_0$ and $x_2 = x_1 + 0.025$. The circular frequency of excitation is $\omega_{3D} = 150$, and the actuator width in the spanwise direction is bounded by $z_1 = -0.01$ and $z_2 = 0.01$. A random background perturbation field with an RMS of $O(1 \times 10^{-4})$ is also included in the actuator to enhance the stochastic nature of simulations that may reach post-breakdown conditions (Sayadi, Hamman & Moin 2013). To localize the wavepacket in time, the actuator is turned off after two time periods of the wave, by bounding the perturbation input within the time interval, $0 \leq t \leq 4\pi/\omega_{3D}$.

The overall effects of wall cooling and supersonic modes on transition are first qualitatively summarized in figure 11. The eventual state of the wavepacket near the exit of the computational domain ($x_{NC} \sim 4$) is presented for four of the wall temperatures simulated, $T_W = 7, 3, 0.5$ and $T_W = 0.1$. Vortical structures as defined by the Q-criterion, coloured by streamwise velocity, u, are used to visualize the wavepacket. The wavepacket in the near-adiabatic wall, $T_W = 7$, attenuates outside the region of linear instability without tripping the HBL (figure 11*a*). The low value of the Q-criterion ($Q = 1$) reflects this state, and the wavepacket retains the signature of 2-D waves injected into the flow by the actuator. In the moderately cooled wall, $T_W = 3$, the second mode is destabilized due to wall cooling, but as observed in the context of figure 9, does not radiate. This yields stronger amplification of the wavepacket, and it develops into a 'young turbulent' spot (Sivasubramanian & Fasel 2010) by the end of the domain, as seen in figure 11(*b*), with hairpin vortices trailing the leading 'core' region. The vortical structures in this turbulent spot are thus highlighted using a higher threshold, $Q = 100$.

The cases $T_W = 0.5$ and $T_W = 0.1$ account for the impact of radiative efflux of energy. Here, the second mode is even more destabilized, but also radiates vortical and acoustic components of energy into the free stream (as seen in figure 9). Figures 11(*c*) and 11(*d*) clearly indicate that these highly cooled HBLs undergo transition due to the amplification and breakdown of the respective wavepacket, giving rise to well-defined turbulent spots.

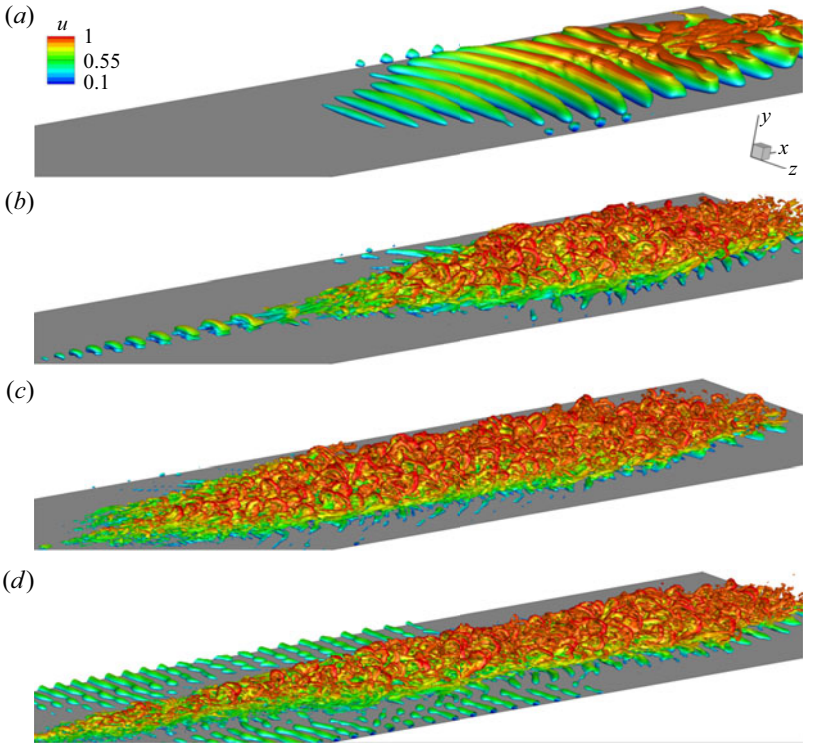

Figure 11. Instantaneous vortical structures induced by the wavepacket, visualized using Q-criterion, coloured by u. Results obtained when the perturbations reach the exit of the computational domain in each case. Plots for (*a*) $T_W = 7$, (*b*) $T_W = 3$, (*c*) $T_W = 0.5$ and (*d*) $T_W = 0.1$. All panels display identical contour levels, as indicated in (*a*). (*a*) $T_W = 7,\ Q = 1,$ (*b*) $T_W = 3,\ Q = 100,$ (*c*) $T_W = 0.5, Q = 100,$ (*d*) $T_W = 0.1, Q = 100$.

Despite radiative losses, wall cooling is observed to increasingly enhance the development to turbulence by second-mode wavepackets, resulting in elongated turbulent spots that sustain fine-scale features. The turbulent spots also become 'flatter' over the cooler walls, since they are confined to thinner boundary layers. Although 3-D simulations were performed for $T_W = 7, 3, 1, 0.5, 0.3$ and $T_W = 0.1$, for brevity, key trends are summarized in the following discussion using the most illustrative cases. For example, many of the inferences regarding transition are reported using only the two extreme cases, $T_W = 3$, and $T_W = 0.1$, where the respective HBLs trip. Additional cases are included selectively to enhance the clarity of those trends.

5.2. *Waveform evolution and spectra*

The spatio-temporal evolution of the wavepacket is summarized using wall-pressure perturbations in figure 12, for the cases, $T_W = 7, 3, 0.5$ and $T_W = 0.1$.In each plot the horizontal axis spans $0 \leq x_{NC} \leq 4$, and the vertical axis is a relative measure of fluctuating pressure, p'_N, which is p' normalized by its peak value at the reference time instant, $t_0 = 1$. As observed in the isolevels of figure 11(*a*), although the actuator amplitude for $T_W = 7$ is large enough to introduce nonlinear perturbations in the HBL (Egorov *et al.* 2006; Hader & Fasel 2019), the forcing profile chosen results in eventual attenuation in the downstream direction, without tripping the HBL. Here $T_W = 3$ shows higher

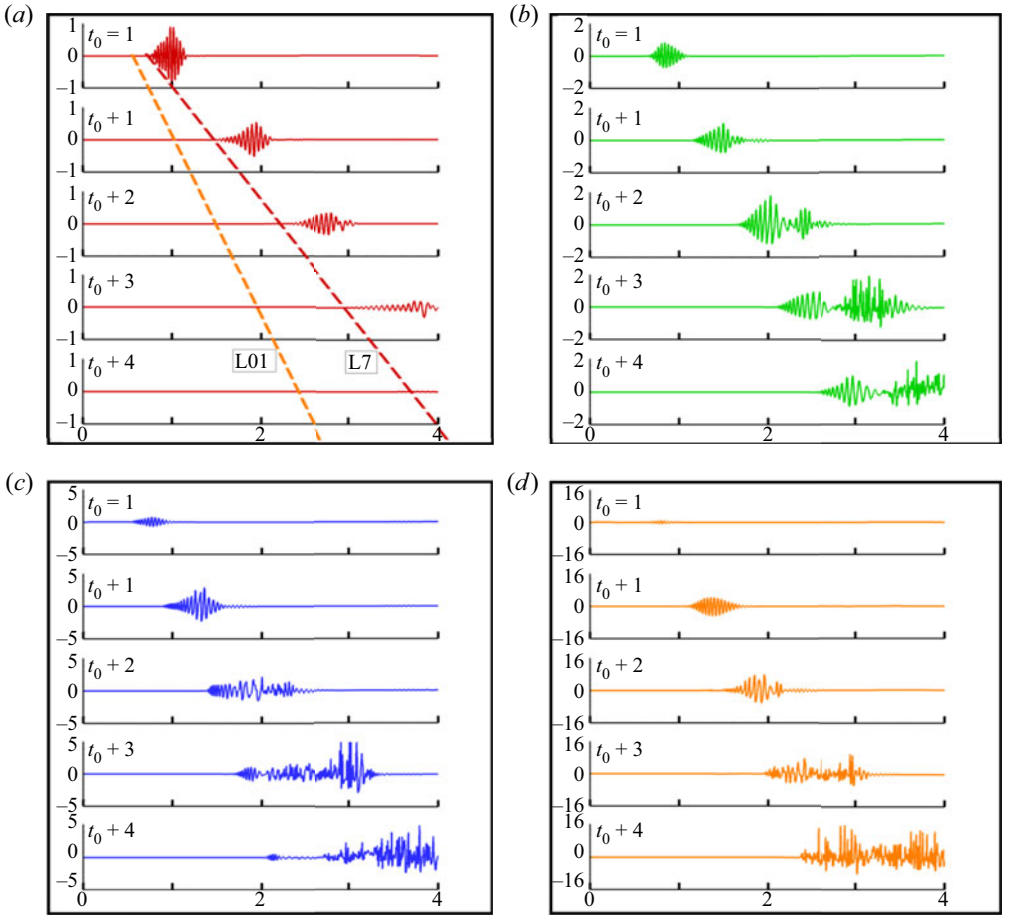

Figure 12. Streamwise distribution of wall-pressure perturbations at the indicated time instances for (*a*) $T_W = 7$, (*b*) $T_W = 3$, (*c*) $T_W = 0.5$ and (*d*) $T_W = 0.1$. The dashed inclined lines in (*a*), L01 and L7, trace the trailing edges of the wavepackets in $T_W = 7$ and $T_W = 0.1$, respectively, to estimate their convective speeds. (*a*) p'_N vs. x_{NC}, $T_W = 7$, (*b*) p'_N vs. x_{NC}, $T_W = 3$, (*c*) p'_N vs. x_{NC}, $T_W = 0.5$, (*d*) p'_N vs. x_{NC}, $T_W = 0.1$.

amplification in the downstream direction, and by time $t = t_0 + 1$, the wavepacket exhibits an early signature of an amplitude modulation at its leading edge. In the following snapshots, this leading, modulated envelope develops into a highly nonlinear region, with rapid amplification of perturbations. The nonlinear region progressively moves away from the trailing wavepacket, consistent with experimental observations (Glezer, Katz & Wygnanski 1989), and eventually becomes the 'turbulent core' (Casper, Beresh & Schneider 2014) of a young turbulent spot.

Qualitative differences emerge in the evolution of the wavepackets when the wall is highly cooled. Nonlinear effects modulating the wavepacket envelopes do not clearly demarcate a leading head and a trailing region. This demarcation weakens as the wall is progressively cooled (see figures 12*c* and 12*d*). In these cases, significant streamwise elongation of the wavepackets occurs, and the leading front is followed by several intermittent turbulent regions. Cooling also decreases the convective speed of the wavepacket, as is evident by comparing the positions of the leading and trailing edges at different time instances for each wall temperature. A rough estimate based on the trailing

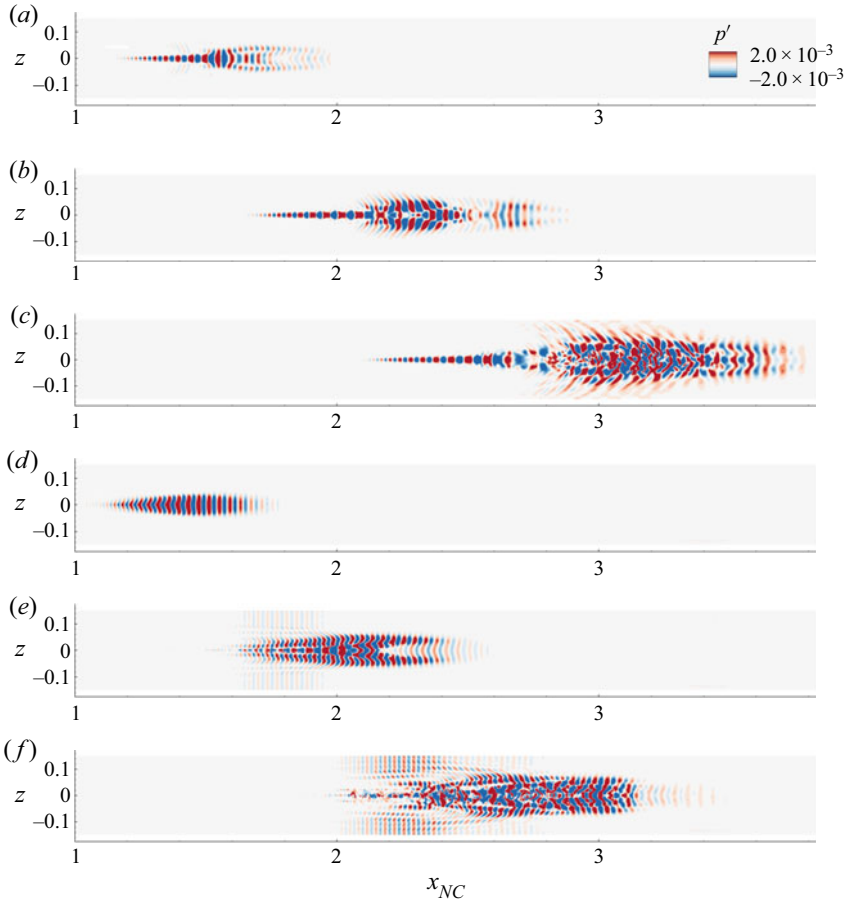

Figure 13. Surface contours of wall-pressure perturbations at the indicated time instances. Plots (*a*,*b*,*c*) correspond to $T_W = 3$. Plots (*d*,*e*,*f*) correspond to $T_W = 0.1$. All panels display identical contour levels, as indicated in (*a*). (*a*) $T_W = 3,\ t_o + 1$, (*b*) $T_W = 3,\ t_o + 2$, (*c*) $T_W = 3,\ t_o + 3$, (*d*) $T_W = 0.1,\ t_o + 1$, (*e*) $T_W = 0.1,\ t_o + 2$, (*f*) $T_W = 0.1,\ t_o + 3$.

edge of the wavepacket in the two extreme conditions, $T_W = 7$ and $T_W = 0.1$, indicates that the convective speed in the latter case is around 63 % that in the former. A graphical comparison of these trends is provided in figure 12(*a*), where *L*7 and *L*01 are the loci of the trailing edges of the wavepacket with $T_W = 7$ and $T_W = 0.1$, respectively. A detailed quantification of trends in convective speeds is presented later in § 5.3.

The spanwise structure of the wavepackets is now examined using wall-pressure perturbation contours in figure 13. To highlight the effect of cooling on wavepacket breakdown processes, two cases, $T_W = 3$, and $T_W = 0.1$, are chosen at three intermediate time instances, included earlier in figure 12. Comparing figures 13(*a*) and 13(*d*), $T_W = 3$ exhibits relatively prominent oblique waves and a nascent head region, whereas $T_W = 0.1$ is still dominated by 2-D second-mode waves at $t = t_0 + 1$. At the next instant shown (figure 13*b*), the warmer wall displays a clear demarcation of the head region in the wavepacket, which bifurcates along the centre, and contains oblique waves on the outer edges, resulting in lateral spreading. This feature was also seen in experimental wall-pressure perturbations of early turbulent spots in a hypersonic nozzle wall by

Casper *et al.* (2014). At the corresponding time instant in the cooler HBL (figure 13*e*), the 2-D structures at the centre of the wavepacket show early signs of disintegration. At $t = t_0 + 3$, the head region of the warmer wavepacket has already disintegrated into a turbulent spot as seen in figure 13(*c*), with significant asymmetry about the mid-span. Oblique waves also amplify along its edges, widening the spot considerably.

When $T_W = 0.1$, although a head region is not conspicuous at $t = t_0 + 3$, the major portion of the wavepacket undergoes disintegration into an elongated turbulent spot, with little trace of the 2-D waves within (figure 13*f*). However, unlike for the warmer wall, this wavepacket contains 2-D waves outside its edges, which are prominently observed in $2 \leq x_{NC} \leq 2.75$. This is consistent with predictions of linear theory, according to which 2-D waves increasingly amplify with wall cooling.

The corresponding spanwise wavenumber spectra are provided in figure 14. In each panel, only the half-plane of the spanwise wavenumber (β) axis is included due to its symmetry. This is then augmented by a half-plane visualization of the $x - z$ distribution of the wavepacket (discussed above in figure 13) for easy reference. For clarity, the instantaneous spanwise spectra are also averaged locally across a time window, $t \pm \Delta t$, where $\Delta t = 0.038$. Comparison of figures 14(*a*) and 14(*b*) confirms a stronger presence of 2-D second-mode waves over the cooler plate. Following the formation of the head region in the warmer wavepacket, a second energy peak appears at $\beta \sim \pm 93$, as indicated by the arrow A1 in figure 14(*c*). This is about half the value of the streamwise wavenumber, α, of the amplified second-mode instability (see, e.g. inset *a*1 in figure 7). The cooler wavepacket displays a more continuous range of excited wavenumbers, with peaks at $\beta \sim \pm 93$ and near its superharmonic, $\beta \sim \pm 196$, which is also marked by arrow A2 in figure 14(*d*). At later stages of development, both the warmer and cooler wavepackets exhibit a wider range of spanwise wavenumbers (figures 14(*e*) and 14(*f*), respectively). However, the cooler wavepacket has relatively more energy content at high wavenumbers, and extends across almost twice the spanwise spectrum of the warmer wavepacket. Consequently, the turbulent spots formed over cooler walls are expected to sustain smaller scales of turbulence, relative to the warmer wall. This trend is further addressed below, in the context of intermittent events in the wake of the head region.

The spatio-temporal signature of a wavepacket is relatively localized. Spectral analyses of such signals are best accomplished by a time-frequency approach, e.g. a scalogram, using a wavelet transformation. Yates, Tufts & Juliano (2020) have recently utilized this technique to identify localized features of stationary cross-flow vortices over a hypersonic cone. In addition to its localized nature, perturbations in the wavepacket are also qualitatively different in the leading and trailing regions, which precludes statistical stationarity (in time) of the signal. Thus, to quantify the spectral characteristics of wavepacket evolution at different wall temperatures, the scalogram of wall-pressure perturbations is examined at various streamwise locations along the mid-span.

The trends are summarized in figure 15 using the results for $T_W = 3$ (left column) and $T_W = 0.1$ (right column).The horizontal axis is time, and the vertical axis is circular frequency, i.e. the pseudo-frequency obtained from the scale-to-frequency conversion relation of the Morlet wavelet used for the transformation. Contour values represent the wavelet coefficient at a given time-frequency coordinate. For reference, the forcing frequency ($\omega = 150$) and its subharmonic ($\omega = 75$) are also marked using dashed lines in each panel. The wavepacket is essentially centred around the forcing frequency at upstream locations closer to the actuator. Therefore, results are reported at relatively downstream locations, $x_{NC} = 1.5, 2, 3$ and $x_{NC} = 4$, where nonlinear effects induce significant variations in the spectra.

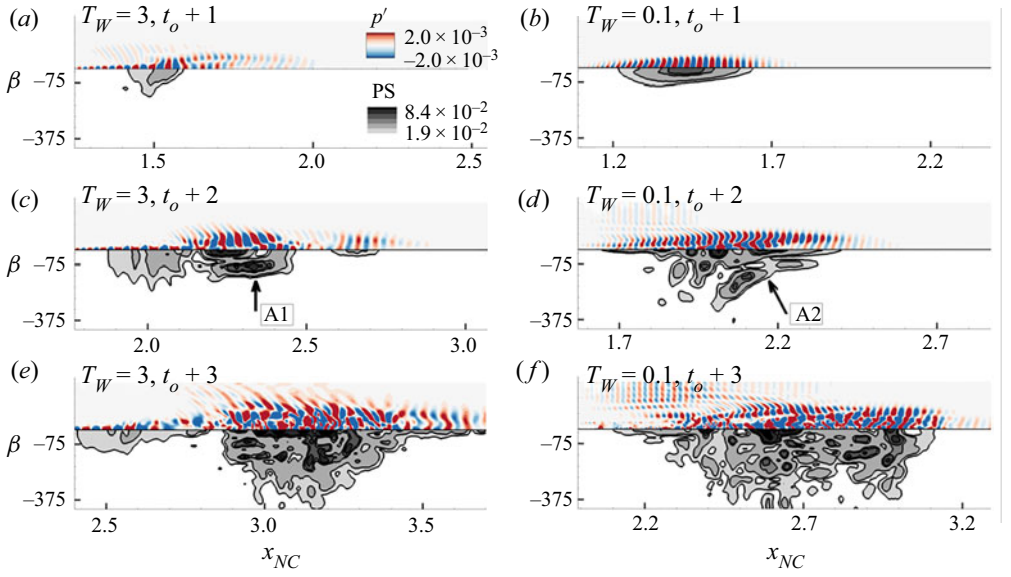

Figure 14. Spanwise wavenumber (β) spectrum obtained as a function of streamwise distance, at the indicated time instances. Plots (*a*), (*c*) and (*e*) correspond to $T_W = 3$. Plots (*b*), (*d*) and (*f*) correspond to $T_W = 0.1$. In each panel, the half-plane of the spectral (vertical) axis is overlaid with the half-plane of the wall-pressure perturbations shown earlier in figure 13. Arrows A1 and A2 highlight relevant features in respective panels. All panels display identical contour levels, as indicated in (*a*).

At $x_{NC} = 1.5$ (figures 15*a* and 15*b*) wavepackets at both wall conditions are still localized, but show the presence of lower frequencies than those of the forcing. The shift in peak energy is towards the subharmonic, $\omega = 75$. Although localized, the cooler wall HBL already shows early signs of higher frequencies as well, particularly at locations of high wavepacket amplitudes. Moving downstream, the streamwise elongation in the wavepackets is primarily observed near the subharmonic, as depicted by figures 15(*c*) and 15(*d*). The warmer wall wavepacket appears relatively coherent, and the energy at higher frequencies is localized in a zone (marked with arrow A1), which eventually bifurcates into the head region. The cooler wall wavepacket is more dispersive, and higher frequencies are excited at multiple locations, some of which are marked by arrows A2, indicating a stronger presence of nonlinearities. At $x_{NC} = 3$, figure 15(*e*), the head region of the warmer wall wavepacket, i.e. that appearing earlier on the time axis, is detached from the trailing region, and contains most of the higher broadband frequencies, suggesting its evolution into an early turbulent spot. The peak in the higher frequencies at $\omega \sim 230$ (arrow A3) is characteristic of a nonlinear interaction between the forcing frequency and its subharmonic, resulting in the quadratic interaction, $\omega_1 + \omega_2 = \omega_3$, with $\omega_1 = 150$, $\omega_2 = 75$ and $\omega_3 = 225$. The trailing region continues to display a harmonic nature, with a compact frequency distribution. The cooler wall wavepacket does not exhibit a prominent head region (figure 15*f*), but contains a series of energetic events, which have broader spectral content than the warmer wall case. This shows that wall cooling results in more rapid development of intermittent turbulence in the wake of the head region, and populates the fine-scale region of the spectrum. Further towards the outflow ($x_{NC} = 4$), the warmer wavepacket forms a turbulent spot in the leading region, and accounts for most of the energetic perturbations (figure 15*g*). The cooler wavepacket in figure 15(*h*) has a longer temporal extent with sustained turbulence in the wake of the

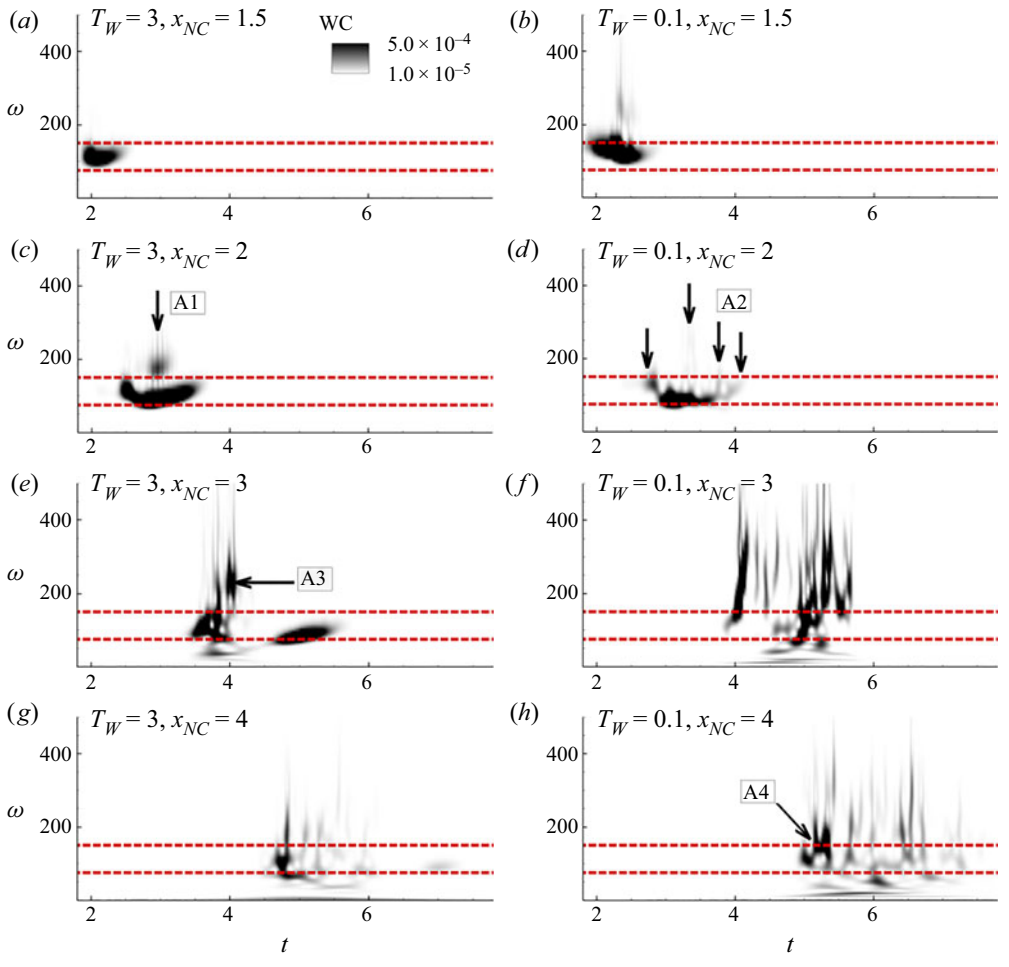

Figure 15. Time-frequency signature of wavepacket evolution represented using scalograms of wall-pressure perturbations on the mid-span, at indicated streamwise locations. Plots (*a*), (*c*), (*e*) and (g) correspond to $T_W = 3$. Plots (*b*), (*d*), (*f*) and (*h*) correspond to $T_W = 0.1$. The upper and lower dashed horizontal lines mark the forcing frequency and its subharmonic, $\omega = 150$ and $\omega = 75$, respectively. Arrows A1, A2, A3 and A4 highlight relevant features in respective panels. All panels display identical contour levels, as indicated in (*a*).

leading spot. The relative dominance of the forcing frequency in the leading region of the cooler wavepacket (arrow A4) is again consistent with the destabilization of second-mode instability due to wall cooling. Prior high-fidelity simulations (Krishnan & Sandham 2006; Redford *et al.* 2012) have observed a progressive dominance of second-mode waves in turbulent spots with increasing Mach numbers. The current analysis shows that, even under breakdown scenarios at hypersonic speeds, turbulence spots in cooler boundary layers retain a stronger presence of the initiating linear instabilities, particularly in the leading region.

The intermittently energized frequency spectrum trailing the head region also results in spatial scale variations in the boundary layer. This is evaluated using the time-accurate spanwise wavenumber distribution near the outlet of domain $x_{NC} = 4$. Results are provided in figure 16 for $T_W = 3$ and $T_W = 0.1$ using wall-pressure perturbations.The corresponding scalograms (discussed above in figures 15*g* and 15*h*) are also reproduced

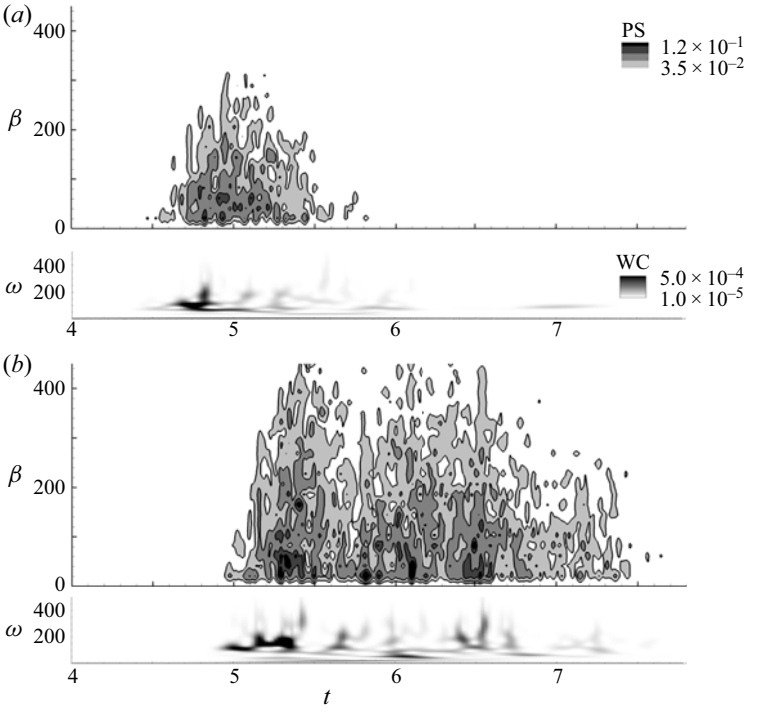

Figure 16. Spanwise wavenumber spectrum obtained as a function of time for (*a*) $T_W = 3$ and (*b*) $T_W = 0.1$, near the exit of the computational domain, $X_{NC} = 4$. In each panel, the wavenumber spectrum is augmented with the corresponding pressure scalogram on the mid-span. Contour levels displayed are indicated in (*a*).

again for easy reference. Note that in order to highlight the 3-D nature of the waves, the zero wavenumber component has been removed from the spanwise signal prior to obtaining the spectrum. Consistent with the frequency signature, the spatial scales in the warmer wall wavepacket are most energetic and display broadband behaviour only in the head region (figure 16*a*). No significant energy content is evident in the oblique waves after the compact head region convects out of the domain. The cooler wall wavepacket on the other hand has a longer signature on the exit plane, as seen in figure 16(*b*). Intermittent spurts of energy in the frequency spectrum are accompanied by the corresponding generation of 3-D structures in the boundary layer. The presence of higher wavenumbers in the cooler wall wavepacket confirms the presence of fine-scale features in these boundary layers.

5.3. *Characteristic features of wavepackets*

A clear understanding of formation and evolution of wavepackets is crucial to the accurate prediction and control of transition pathways in high-speed boundary layers. Characterization of their key features and statistics also aide in modelling their impact on the boundary layer. For example, measured spatio-temporal correlations were used by Park & Lauchle (2009) to model wall-pressure perturbations in transition zones of subsonic boundary layers. We now identify some important physical features of the wavepackets and turbulent spots generated in the cooled HBLs.

The 3-D structures in the $T_W = 3$ and $T_W = 0.1$ wavepackets are shown in figure 17(a) and 17(b), respectively.Vortical features are visualized using the Q-criterion, coloured by the streamwise velocity component. For both cases, views of the turbulent spots from beneath (BV), top (TV), side (SV) and front (FV), i.e. looking upstream from the outflow boundary, are provided for clarity. Comparing SV and FV, it is evident that the turbulent spots over warmer walls protrude higher into the free stream, due to thicker boundary layers in the corresponding laminar profiles. As seen in the BV, both wavepackets contain spanwise coherent structures near the wall, which have been associated with second-mode instabilities (Jocksch & Kleiser 2008). In both wavepackets, these spanwise structures are most dominant near the leading edge of the spot, which is consistent with the presence of the second-mode frequency in the scalogram at the corresponding location (see discussion of figure 15g). The lateral spreading half-angle of the turbulent spot over the warmer wall is approximated by the dotted lines, subtending an angle of 4°, with the horizontal axis. This is consistent with experimental (Fischer 1972) and computational estimates (Redford *et al.* 2012). Although the cooler wall HBL has a longer and more slender turbulent spot, the spreading rate is apparently reasonably well approximated by the same angle. Considering that the wall temperature is reduced by over an order of magnitude compared with the warmer wall, this suggests that the edge Mach number has a more prominent influence, compared with wall thermal conditions, on the lateral spread rate. The spatial coherence of outer boundary layer structures is also different in the two spots, as seen from the TV images. The warmer wall tends to sustain hairpin vortices that exhibit larger spanwise extent, compared with the cooler wall, where these vortices are disintegrated. This is also consistent with the dominance of energy in higher β-values, observed in the spanwise spectrum of the cooler wall HBL in figure 16(b).

A measure of the coherence in above vortical structures can be obtained from the trends in streamwise vorticity, ω_x. These also provide information about near-wall effects of coherent structures as reported by Hader & Fasel (2019), who analysed streamwise vorticity contours and the baroclinic vorticity production term to explain the observed skin friction and heat transfer peaks over a hypersonic flared cone. The energetically dominant vortical structures (as represented by streamwise vorticity) in the turbulent spots formed in $T_W = 3$ and $T_W = 0.1$ are extracted using the proper orthogonal decomposition (POD) technique (Lumley 1967).The results are provided in figure 18. Proper orthogonal decomposition is performed on the three component velocity field on the exit plane defined by $x_{NC} = 4$, $0 \leq y \leq 0.05$ and $-0.15 \leq z \leq 0.15$. The method of snapshots (Sirovich 1987) utilizes data on this plane during the time interval when the turbulent region in the spot passes through. Figures 18(a) and 18(b) represent the contours of ω_x on the exit plane at $x_{NC} = 4$, and its spanwise spectrum obtained at each wall-normal location, respectively, for $T_W = 3$. The vorticity contours are created from the leading velocity POD mode (excluding the temporal mean), and are denoted ω_x(POD1). Figures 18(c) and 18(d) are the corresponding results for $T_W = 0.1$. While the leading mode in $T_W = 3$ accounts for around 35 % of the energy content, that in $T_W = 0.1$ constitutes approximately 25 %. This is due to the more advanced state of the breakdown of the spot in the cooler HBL, which shifts the system away from low-rank behaviour. The vortical structures in $T_W = 0.1$ have a peak energy closer to the wall ($y_{\beta M} \sim 0.05$) than those in $T_W = 3$($y_{\beta M} \sim 0.1$), which can result in higher shear (discussed below) on the surface. The cooler HBL also has more instances of high-vorticity events near the wall, as indicated by the vorticity contours. The dominant vortical mode also contains more fine-scale features in $T_W = 0.1$, which are evident by comparing the spectra in figures 18(b) and 18(d). Most of the high-shear events

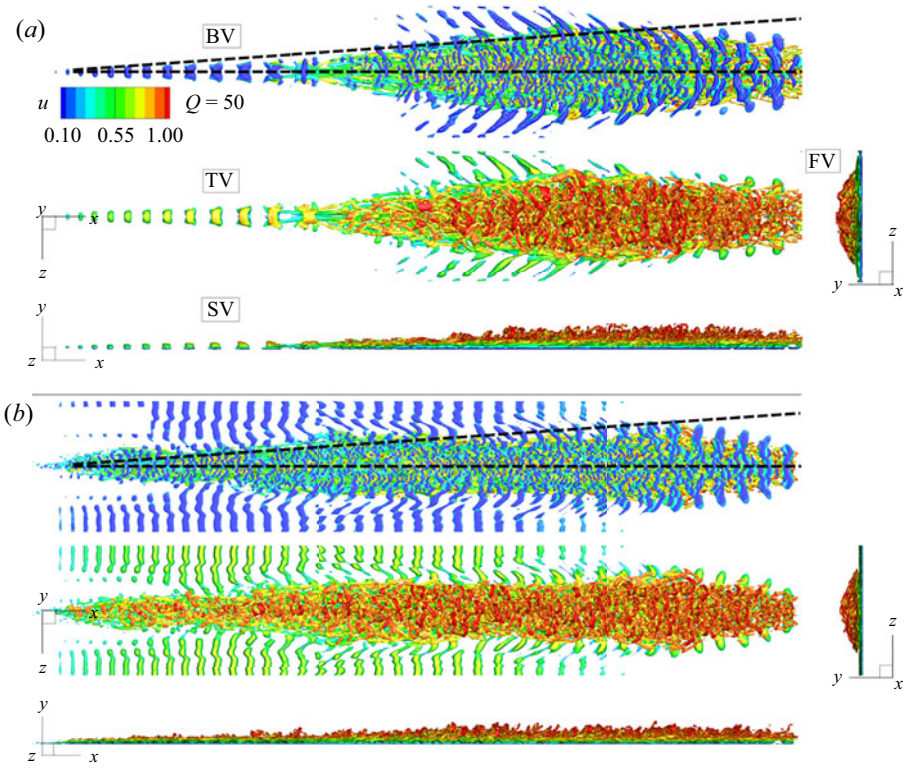

Figure 17. Physical structure of the turbulent spots generated in (*a*) $T_W = 3$ and (*b*) $T_W = 0.1$, as seen in primary views, visualized using Q-criterion, coloured by u. The two dashed lines in the top view of each panel mark a 4° angle with the horizontal axis. All panels display identical contour levels, as indicated in (*a*).

exist below the laminar boundary layer height, δ_{99}, as marked in the figures. This confirms the 'flattening' of the turbulent spot in cooler HBLs, as seen earlier in the isolevels of Q-criterion in figures 11 and 17.

The cooler turbulent spot appears more slender and elongated in figure 17, compared with the warmer case. This could suggest variations in the lateral spreading mechanism active in these HBLs. Redford *et al.* (2012) identify near-wall regions of spanwise-velocity peaks, which could widen the spot by forming lateral jets. The effect of wall cooling on this mechanism is analysed in figure 19 by using spanwise-velocity variations.To ensure statistical relevance, the associated features are obtained using the leading spanwise-velocity POD mode, marked w(POD1). Results for $T_W = 3$ and $T_W = 0.1$ are provided in figures 19(*a*) and 19(*b*), respectively. As observed in the vorticity fields above, the spanwise velocity also contains relatively larger length scales in the warmer boundary layer. Towards the extremities of the span ($z \sim \pm 0.15$), $T_W = 3$ displays coherent regions of velocity perturbations, consistent with an outward motion from the centreline. Such a coherent feature is absent in the cold case. Enhanced turbulent breakdown of spanwise coherent structures and relatively high wavenumbers near the wall (see figure 18*d*) could weaken this mechanism, thus generating a relatively slender spot. A detailed view of the lateral jet (marked by the dashed rectangle in figure 19*a*) in the warmer spot is provided in figure 19(*c*), along with the vector field, (w, v), formed by its leading POD modes. The lateral jets originate from near the centreline of the spot and extend to its extremities. The upwash of low-momentum fluid from near the wall to the outer edges is

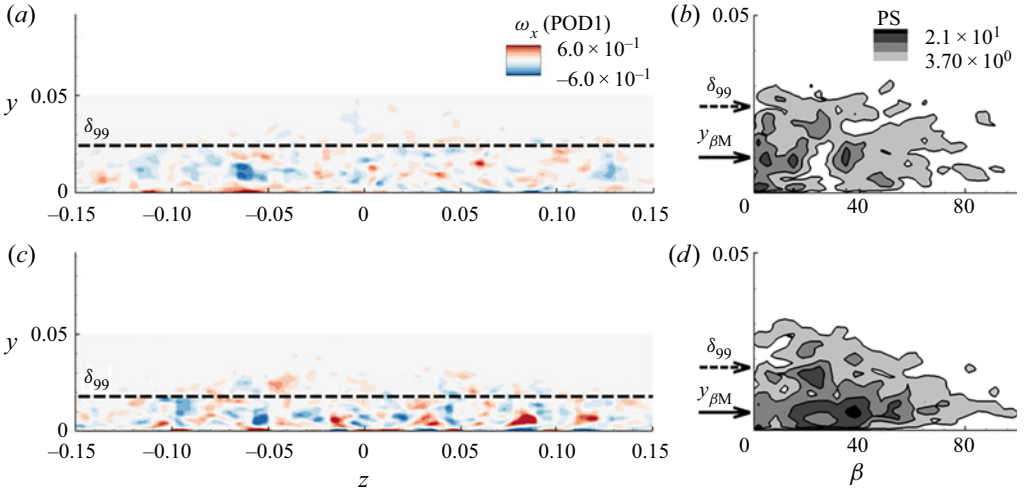

Figure 18. (*a*) Contours of streamwise vorticity, ω_x, as observed on the exit plane, $x_{NC} = 4$, in the leading POD mode for $T_W = 3$. (*b*) Spanwise wavenumber spectrum of the vorticity field, obtained as a function of wall-normal distance. Plots (*c*) and (*d*) show the corresponding results for $T_W = 0.1$. The horizontal dashed lines in (*a*) and (*c*) mark the laminar boundary layer thickness, δ_{99}. The arrows on the vertical axes in (*b*) and (*d*) mark δ_{99} and the location of the peak in the spanwise spectrum, $y_{\beta M}$. Panels (*a*) and (*c*) display identical contour levels, as indicated in (*a*). Panels (*b*) and (*d*) display identical contour levels, as indicated in (*b*). (*a*, *b*) $T_W = 3$, (*c*, *d*) $T_W = 0.1$.

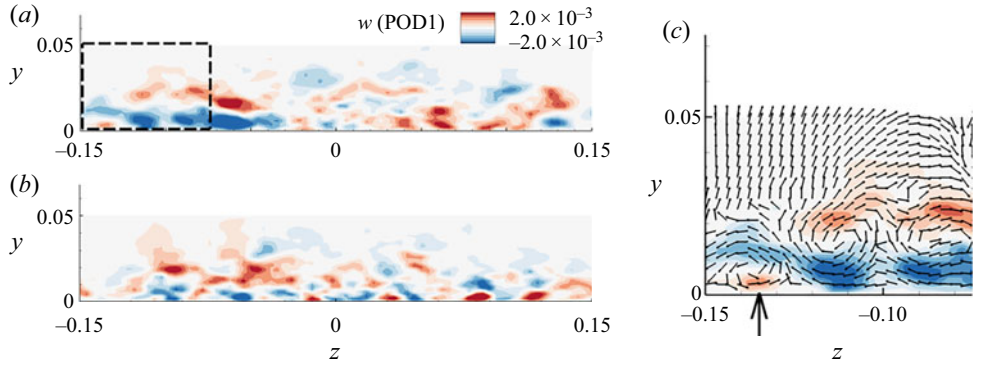

Figure 19. Contours of spanwise velocity, w, as observed on the exit plane, $x_{NC} = 4$, in the leading POD mode for (*a*) $T_W = 3$ and (*b*) $T_W = 0.1$. The region marked by the dashed rectangle in (*a*) is magnified in (*c*). The vector field in (*c*) corresponds to (w, v), as defined in the leading POD mode. The arrow on the horizontal axis in (*c*) marks a vortex beneath the lateral jet. All panels display identical contour levels, as indicated in (*a*).

evident in this field. Streamwise vortices exist above and beneath the lateral jet, which are accompanied by movement of fluid into the core of the spot. The vertical arrow marks a streamwise vortex beneath the lateral jet, resulting in the injection of near-wall flow into the turbulent spot. This is consistent with the observations from instantaneous ω_x-snapshots by Redford *et al.* (2012) for a Mach 3 hot wall boundary layer.

An important feature of wavepackets and the succeeding turbulent spots is their convective speed. Trends in this property are summarized in figure 20 using results from $T_W = 3$, $T_W = 0.5$ and $T_W = 0.1$.The chronogram of wall-pressure perturbations along the mid-span for $T_W = 3$ is shown in figure 20(*a*). The solid outline marks the

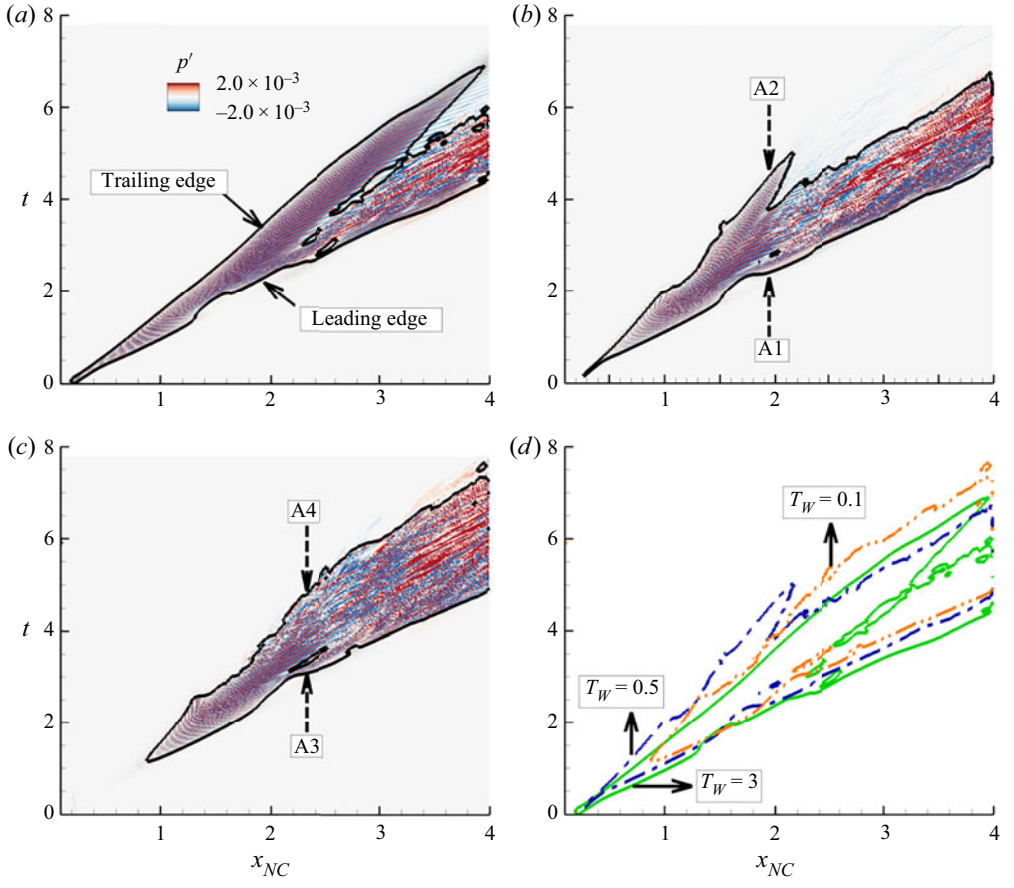

Figure 20. Chronogram of wall-pressure perturbations on the mid-span for (*a*) $T_W = 3$, (*b*) $T_W = 0.5$ and (*c*) $T_W = 0.1$. The solid contour lines in (*a*), (*b*) and (*c*) trace the envelope of the evolving wavepackets. These three envelopes are overlaid in (*d*). Arrows A1, A2, A3 and A4 highlight relevant features in respective panels. Panels (*a*), (*b*) and (*c*) display identical contour levels, as indicated in (*a*).

envelope of the wavepacket at each time instant, using a predefined threshold, $|p'| = 2 \times 10^{-3}$. Figures 20(*b*) and 20(*c*) are the corresponding results for $T_W = 0.5$ and $T_W = 0.1$, respectively. Figure 20(*d*) superimposes the envelopes from these three cases for comparison. The leading edges of the wavepackets have smaller slopes, $\Delta t/\Delta x_{NC}$, compared with the corresponding trailing edges, suggesting a higher convective speed in all cases. For $T_W = 3$, the leading and trailing edges convect at approximately 85 % and 55 % of the free stream velocity, respectively, which is consistent with prior experimental and computational estimates (Wygnanski, Sokolov & Friedman 1976; Wygnanski, Zilberman & Haritonidis 1982; Jocksch & Kleiser 2008).

Prior to addressing the effect of wall cooling on the propagation speed, it is essential to account for the dynamical variations induced on the streamwise structure of the wavepackets. The outline of the envelope for $T_W = 3$ indicates a clear bifurcation of the wavepacket into two zones, at $(x_{NC}, t) \sim (2.5, 3.8)$, which form the head and the trailing regions, earlier identified in the time-frequency analysis (see, e.g. figure 15*c*). While the head region has a chaotic imprint due to the broadband nature of its constituent frequencies and oblique modes, the trailing region is relatively well ordered, due to its harmonic nature,

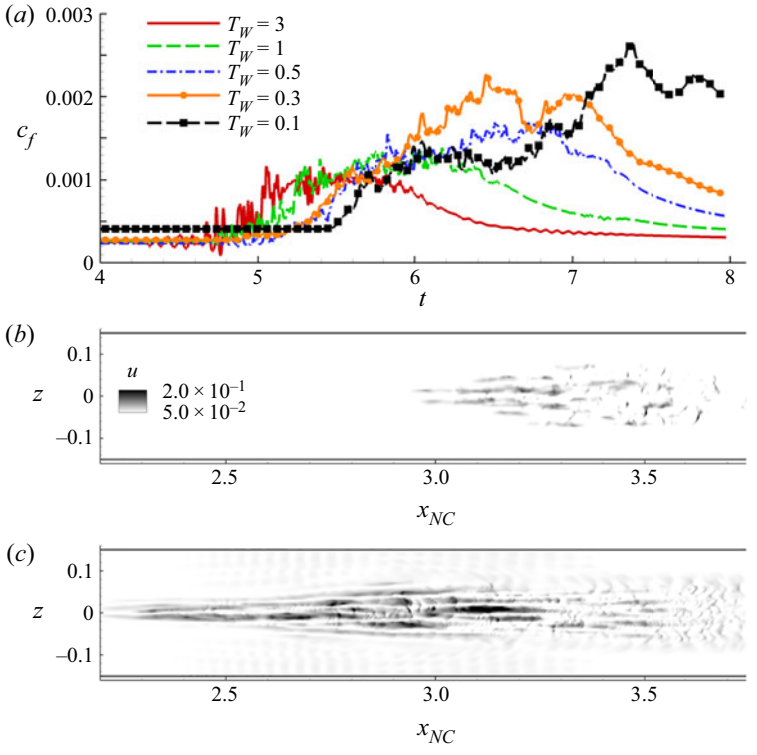

Figure 21. (*a*) Temporal evolution of spanwise averaged skin friction coefficient, c_f, at $x_{NC} = 4$, for various cold walls. Instantaneous near-wall contours of streamwise velocity for (*b*) $T_W = 3$ and (*c*) $T_W = 0.1$. Panels (*b*) and (*c*) display identical contour levels, as indicated in (*b*).

and is dominated by the subharmonic of the forcing frequency. In cooler wall HBLs, this trailing zone is progressively curtailed, as seen from the trends in figures 20(*a*)–20(*c*). The streaks in the turbulent head region emerge as the major component of the wavepacket trace in the cooler walls, and exhibit a different convective speed than the precursor harmonic wavepacket. This switch in the convective speeds is highlighted by two vertical dashed arrows; A1 and A2 in figure 20(*b*), and A3 and A4 in figure 20(*c*). The convective speeds of the leading edges increase by around 10 % in the cooler walls after initiation of breakdown. The trailing edges exhibit a more dramatic increase, by over 60 %.

5.4. *Wall loading*

Wavepackets that cause transition in HBLs result in increased drag and thermal loads on the surface. The impact on drag due to wall cooling is assessed in figure 21. Since the qualitative aspects of the wavepacket evolve rapidly, the results are visualized in a time-accurate manner near the exit plane of the computational domain, at $x_{NC} = 4$, in figure 21(*a*). The quantity plotted is the coefficient of skin friction, c_f, defined as

$$c_f = \frac{2}{Re}\mu \left.\frac{\partial u}{\partial y}\right|_{y=0}. \tag{5.3}$$

The coefficient is averaged in the spanwise direction as well. To summarize the trends, data from all the HBLs that transitioned are included here. Note that c_f increases from

the laminar values as the turbulent spot approaches the exit plane, e.g. $t \sim 4.5$ in the case $T_W = 3$. This is also the location where the leading edge envelope intersects $x_{NC} = 4$ in figure 20(a). For the cooler walls, the c_f increase begins at later time instants, due to the previously observed slower convective speeds of the respective wavepackets. The peak c_f values at $T_W = 3$ are consistent with those observed for fully turbulent HBLs at adiabatic conditions (Egorov & Novikov 2016). With cooling, the values of c_f increase monotonically, and peak values more than double for the highly cooled cases, $T_W = 0.3$ and $T_W = 0.1$. The temporal distribution of the c_f peaks also changes qualitatively. For $T_W = 3$, the maximum is localized near the leading edge of the spot where dominant hairpin vortices exist. Behind this region, near-wall shear weakens, and is reflected as low values of c_f. In the cooler walls the spots are slender and elongated, thus resulting in a broader hump in c_f. In addition, multiple local peaks are observed due to the intermittent generation of turbulent zones in the wake of the leading spot. Thus, wakes of spots with sustained generation of turbulence have greater impact on wall loading than the spatially localized leading spot observed in the warmer walls.

The distributed impact of cooler wavepackets on the wall is confirmed in figures 21(b) and 21(c), through the near-wall streamwise velocity contours. These velocity fields correspond to the time instant at which vortical features are displayed in figure 17. Compared with $T_W = 3$ (figure 21b), the high-speed streaks in $T_W = 0.1$ (figure 21c) are elongated, and peaks values appear significantly downstream of the leading edge. The higher velocities present in these streaks are evident in the contour levels, and result in increased drag on the surface.

The effects on wall heat transfer are reported in figure 22, which plots the surface heat transfer coefficient, c_h, at $x_{NC} = 4$. Here c_h is defined as (Novikov 2017)

$$c_h = \frac{Q_W^*}{\rho_\infty^* U_\infty^* c_p^* (T_r^* - T_W^*)} = -\frac{\mu_w}{RePr} \frac{1}{(T_r - T_W)} \left.\frac{\partial T}{\partial y}\right|_{y=0}, \tag{5.4}$$

where $Q_W^* = -\mathcal{K}^*(\partial T^*/\partial y^*)|_{y^*=0}$ is the wall heat transfer rate and $\mathcal{K}^*$ is the thermal conductivity. Recovery temperature, T_r^*, is calculated as

$$\frac{T_r^*}{T_\infty^*} = 1 + r\frac{\gamma - 1}{2} M_\infty^2. \tag{5.5}$$

Since the plots are obtained near the exit plane of the breakdown region of the spots, the recovery factor, $r = Pr^{1/3}$.

Typical c_h values in the streaks formed beneath the spot for $T_W = 3$ are about -2×10^{-3}, consistent with turbulent estimates in HBLs (Chynoweth *et al.* 2019). This increases to approximately -3×10^{-3} and -4×10^{-3} for $T_W = 0.5$ and $T_W = 0.1$, respectively. Note that the negative values indicate the presence of relatively warmer fluid near the surface, resulting in heat transfer to the surface. In supersonic boundary layers at near-adiabatic wall temperatures, Krishnan & Sandham (2006) report positive values of c_h (wall cooling) in the calmed region behind the turbulent spot. Although the near-adiabatic case, $T_W = 7$, did not induce a turbulent spot in the current study, we now identify such regions in the cold wall HBLs, which displayed transition. For this, the c_h flood contours are overlaid with the $c_h = 0$ contour using solid lines. For $T_W = 3$ (figure 22a), these zero-contour lines identify regions of wall cooling along the leading regions of the turbulent spot. The 'inrush' (Krishnan & Sandham 2006) of relatively warm fluid in the trailing region of these spots results in wall heating, as opposed to cooling in near-adiabatic cases. Inspection of the topology of these turbulent spots indicates that wall cooling occurs

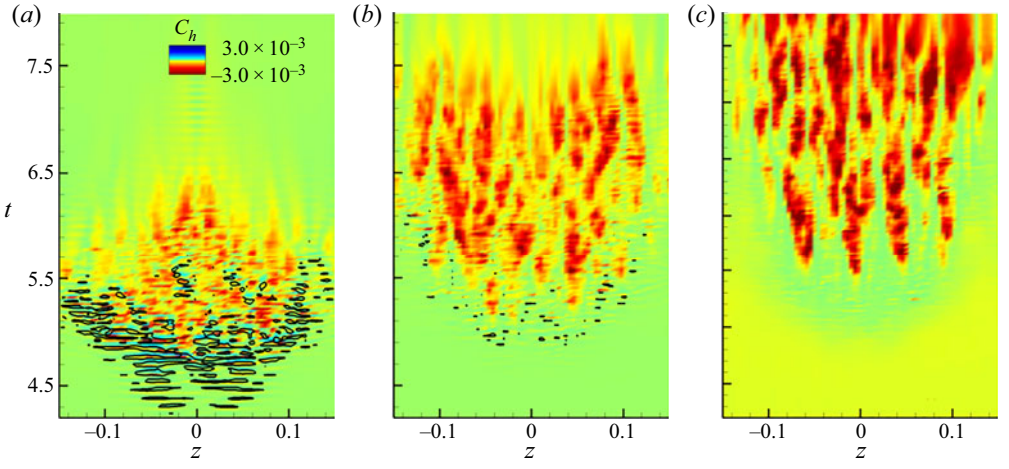

Figure 22. Temporal evolution of surface heat transfer coefficient, c_h, at $x_{NC} = 4$, for (*a*) $T_W = 3$, (*b*) $T_W = 0.5$ and (*c*) $T_W = 0.1$. The solid contour lines in (*a*) and (*b*) mark $c_f = 0$. All panels display identical contour levels, as indicated in (*a*).

immediately behind the near-wall spanwise coherent structures that exist near the leading regions. It results in intense values of positive dilatation, indicating volumetric expansion and cooling of the fluid. As the wall is increasingly cooled, the regions of zero contours diminish as seen for $T_W = 0.5$ and $T_W = 0.1$ in figures 22(*b*) and 22(*c*), respectively. In addition, the trailing streaks become more elongated with higher temperature gradients, resulting in sustained and elevated rates of heat transfer to the surface. Thus, although the leading region of cold wall wavepackets are energetically dominant (see figure 15*h*), peak wall loading occurs in the elongated trailing region. Since the extent of the trailing region is highly dependent on its convective velocity, modelling efforts should accurately account for the variations in its value, as identified in figure 20.

6. Summary

Variations in linear instability mechanisms and flow features due to wall cooling in a HBL at Mach 6 are studied, with particular emphasis on the impact on transition. The dynamics of instability waves associated with wall cooling confirm that over sufficiently cooled walls, the unstable mode F, after synchronizing with the slow continuous acoustic spectrum, switches from a compact form to an oscillatory eigenfunction; this results in supersonic phase speeds in the outer boundary layer and radiation into the free stream. A physical analysis of this supersonic mode using momentum potential theory indicates that radiation from cooled HBLs contains similar acoustic and vortical wave magnitudes. The entropic component is however negligible.

Perturbation analysis of the mean flow associated with varying degrees of wall cooling, using a high-order numerical approach, confirms the observations from linear theory and adds further insight. While the subsonic second mode displays a near-constant wavenumber distribution in the HBL, that in the supersonic mode gradually increases in the outer boundary layer, as it aligns towards the wall. In moderately cooled walls the second mode retains its trapped nature between the wall and the critical layer, as seen previously in near-adiabatic walls. At higher levels of cooling, however, this trapped form ruptures, resulting in efflux of energy into the free stream. This efflux is quantified

by calculating the vortical and acoustic components of the TFE. Although wall cooling increases the radiative loss, there is no apparent reduction of perturbation growth in the HBLs. Increased wall cooling monotonically increases wall-pressure perturbations, in line with the destabilization of the second mode.

The role of supersonic modes, and mean-flow variations due to wall cooling, in inducing realistic transition scenarios are addressed through the study of 3-D wavepacket evolution. The choice of forcing highlights the effect of wall cooling on transition; for the near-adiabatic wall, the second-mode wavepacket of the chosen attributes attenuates after an initial growth region. For cooled HBLs however, the same forcing induces wavepackets that nonlinearly saturate and generate turbulent spots, despite the observed radiative losses. Following the percolation of energy into the subharmonic of forcing frequency, all wavepackets elongate in the streamwise direction, and display a harmonic nature. In moderately cooled walls the next phase involves bifurcation of the wavepacket into a dominant head region and a harmonic trailing region. The head region contains a broadband spectrum, and increasingly displays breakdown of the HBL with wall cooling, eventually resulting in a localized turbulent spot. The highly cooled walls exhibit a qualitatively different scenario, where the wavepackets are significantly more elongated in the streamwise direction. The head region, although energetically dominated by the second-mode forcing frequency, displays a prominent wake, where intermittent local spurts of turbulence are observed. This leads to a broader range of spatio-temporal scales in the cooler wall wavepacket, which are quantified through spectral analyses.

Key physical features of the wavepackets including convective speeds and wall loading are characterized, which can aide in transition model development in cold wall conditions. The moderately cooled wavepackets conform to existing estimates of leading and trailing edge velocities. Once turbulent regions emerge in the highly cooled cases, the convective speed of the trailing edge increases dramatically by over 60 %. The wakes in the highly cooled wavepackets result in significantly elongated near-wall high velocity streaks. These induce sustained values of peak skin friction, that are about twice those reported for adiabatic walls. Heat transfer rates also more than double in the highly cooled walls, and primary regions of wall heating exist in the trailing region of the turbulent spots. Thus, accurate estimates of convective speeds of turbulent spots are critical to reliable wall loading estimates in highly cooled HBLs.

Acknowledgements. The simulations were performed with a grant of computer time from the DoD HPCMP DSRCs at AFRL, NAVO and ERDC, and the Ohio Supercomputer Center.

Funding. This research was supported by the Office of Naval Research (grant: N00014-17-1-2528) monitored by E. Marineau, with R. Burnes serving as technical point of contact.

Declaration of interest. The authors report no conflict of interest.

Author ORCIDs.
S. Unnikrishnan https://orcid.org/0000-0002-8220-9830;
Datta V. Gaitonde https://orcid.org/0000-0001-5400-2560.

Appendix. Grid convergence of results

Grid convergence of the results are addressed by reproducing the nonlinear evolution and eventual breakdown of the wavepacket over the cold wall, using a relatively more refined grid. The 3-D simulation of the coldest wall, $T_W = 0.1$, is chosen for this, since it has the most stringent grid requirements due to the enhanced gradients near the wall, and the presence of finer scales in the boundary layer.

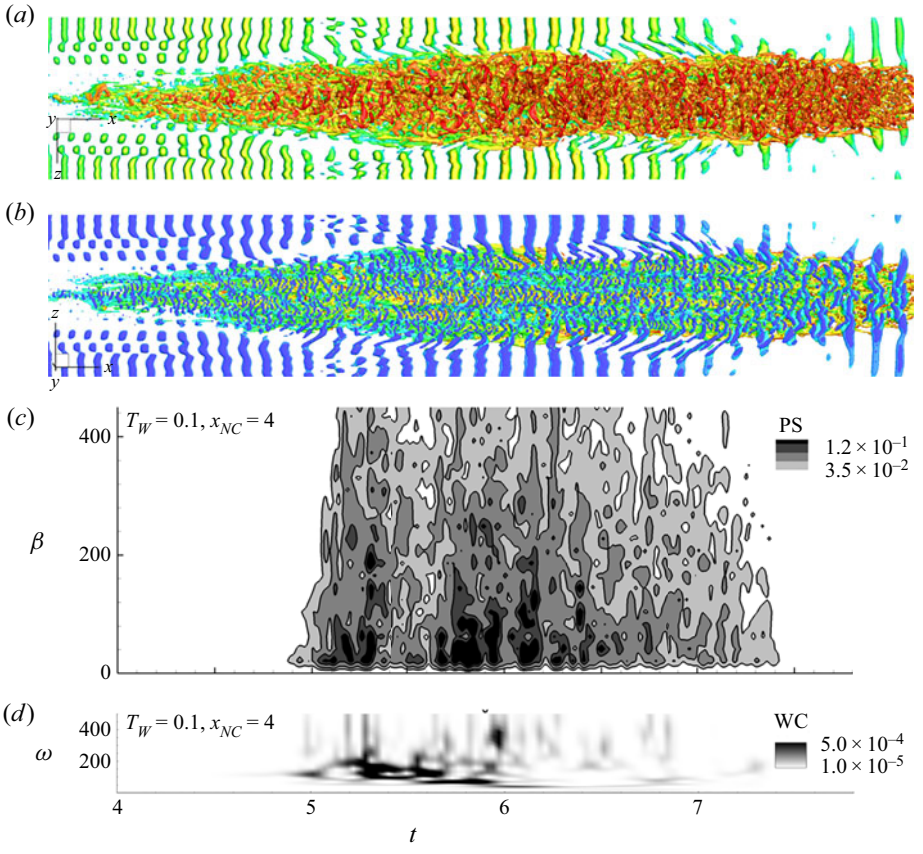

Figure 23. Results obtained for $T_W = 0.1$, using the finer grid, G2. Physical structure of the turbulent spot visualized using Q-criterion, coloured by u – view from the (*a*) top and (*b*) beneath. (*c*) Spanwise wavenumber spectrum obtained as a function of time, near the exit of the computational domain, $X_{NC} = 4$. (*d*) Pressure scalogram on the mid-span at $X_{NC} = 4$.

The convergence study simulates the evolution of the wavepacket with $T_W = 0.1$, on a relatively finer grid, G2, compared with the one reported in § 5 (which is referred to as G1). The grid spacing in G2 is around 15 %, 25 % and 17 % smaller in the streamwise, wall-normal and spanwise directions, respectively, compared with G1. In addition, G2 contains around 21 % more nodes than G1 along the wall-normal direction, within the boundary layer height near the outlet of the computational domain. To address effects of temporal discretization, the time-step size for G2 is reduced by 25 % from that used for G1. The results from this simulation are reported in figure 23. A qualitative visualization of the wavepacket as it approaches the outlet of the domain is provided using Q-criterion, coloured by streamwise velocity, in figures 23(*a*) and 23(*b*). The elongated region of the turbulent spot, and fine-scale features near the wall, are similar to those observed in the computations using grid G1 (see figure 17*b*). Quantitative spectral representations are provided in figures 23(*c*) and 23(*d*), using the spanwise wavenumber spectrum and time-frequency constitution of the wavepacket, respectively. The intermittent nature of turbulence generation in the wavepacket and spectral ranges containing peak energy are reproduced in a consistent manner across the two grids (see also figure 16*b*). The differences between the instantaneous features in the two simulations primarily result from

the stochastic nature of turbulence development in the wavepackets, which is promoted by the trace amounts of random noise added in the forcing. The statistics of wall loading (c_f and c_h), topology of the spots and near-wall streaks in the trailing region of the wavepackets were also ensured to be consistently predicted across both grids. This ensures that key inferences on the evolution of second-mode instability are not significantly affected by the resolution of the grids adopted in this study.

References

Anderson, J.D. 2000 *Hypersonic and High Temperature Gas Dynamics*. AIAA.

Balsara, D.S. & Shu, C. -W. 2000 Monotonicity preserving weighted essentially non-oscillatory schemes with increasingly high order of accuracy. *J. Comput. Phys.* **160** (2), 405–452.

Beam, R. & Warming, R. 1978 An implicit factored scheme for the compressible Navier–Stokes equations. *AIAA J.* **16** (4), 393–402.

Bhagatwala, A. & Lele, S.K. 2009 A modified artificial viscosity approach for compressible turbulence simulations. *J. Comput. Phys.* **228** (14), 4965–4969.

Bitter, N.P. & Shepherd, J.E. 2015 Stability of highly cooled hypervelocity boundary layers. *J. Fluid Mech.* **778**, 586–620.

Casper, K.M., Beresh, S.J. & Schneider, S.P. 2014 Pressure fluctuations beneath instability wavepackets and turbulent spots in a hypersonic boundary layer. *J. Fluid Mech.* **756**, 1058–1091.

Chang, C.-L., Kline, H.L. & Li, F. 2019 Effects of wall cooling on supersonic modes in high-enthalpy hypersonic boundary layers over a cone. *AIAA Aviation 2019 Forum. AIAA Paper* 2019-2852.

Chang, C.-L., Vinh, H. & Malik, M.R. 1997 Hypersonic boundary-layer stability with chemical reactions using PSE. *28th Fluid Dynamics Conference. AIAA Paper* 1997-2012.

Chuvakhov, P.V. & Fedorov, A.V. 2016 Spontaneous radiation of sound by instability of a highly cooled hypersonic boundary layer. *J. Fluid Mech.* **805**, 188–206.

Chynoweth, B.C., Schneider, S.P., Hader, C., Fasel, H., Batista, A., Kuehl, J., Juliano, T.J. & Wheaton, B.M. 2019 History and progress of boundary-layer transition on a mach-6 flared cone. *J. Spacecr. Rockets* **56** (2), 333–346.

Doak, P.E. 1989 Momentum potential theory of energy flux carried by momentum fluctuations. *J. Sound Vib.* **131** (1), 67–90.

Egorov, I.V., Fedorov, A.V. & Soudakov, V.G. 2006 Direct numerical simulation of disturbances generated by periodic suction-blowing in a hypersonic boundary layer. *Theor. Comput. Fluid Dyn.* **20** (1), 41–54.

Egorov, I.V. & Novikov, A.V. 2016 Direct numerical simulation of laminar–turbulent flow over a flat plate at hypersonic flow speeds. *Comput. Maths Math. Phys.* **56** (6), 1048–1064.

Fedorov, A.V. 2011 Transition and stability of high-speed boundary layers. *Annu. Rev. Fluid Mech.* **43**, 79–95.

Fedorov, A.V. & Khokhlov, A.P. 2001 Prehistory of instability in a hypersonic boundary layer. *Theor. Comput. Fluid Dyn.* **14** (6), 359–375.

Fedorov, A.V. & Tumin, A. 2003 Initial-value problem for hypersonic boundary-layer flows. *AIAA J.* **41** (3), 379–389.

Fedorov, A. & Tumin, A. 2011 High-speed boundary-layer instability: old terminology and a new framework. *AIAA J.* **49** (8), 1647–1657.

Fischer, M.C. 1972 Spreading of a turbulent disturbance. *AIAA J.* **10** (7), 957–959.

Glezer, A., Katz, Y. & Wygnanski, I. 1989 On the breakdown of the wave packet trailing a turbulent spot in a laminar boundary layer. *J. Fluid Mech.* **198**, 1–26.

Hader, C. & Fasel, H.F. 2019 Direct numerical simulations of hypersonic boundary-layer transition for a flared cone: fundamental breakdown. *J. Fluid Mech.* **869**, 341–384.

Huang, J., Bretzke, J.-V. & Duan, L. 2019 Assessment of turbulence models in a hypersonic cold-wall turbulent boundary layer. *Fluids* **4** (1), 37.

Jenvey, P.L. 1989 The sound power from turbulence: a theory of the exchange of energy between the acoustic and non-acoustic fields. *J. Sound Vib.* **131** (1), 37–66.

Jocksch, A. & Kleiser, L. 2008 Growth of turbulent spots in high-speed boundary layers on a flat plate. *Intl J. Heat Fluid Flow* **29** (6), 1543–1557.

Knisely, C.P. & Zhong, X. 2019*a* Sound radiation by supersonic unstable modes in hypersonic blunt cone boundary layers. I. Linear stability theory. *Phys. Fluids* **31** (2), 024103.

KNISELY, C.P. & ZHONG, X. 2019*b* Sound radiation by supersonic unstable modes in hypersonic blunt cone boundary layers. II. Direct numerical simulation. *Phys. Fluids* **31** (2), 024104.

KRISHNAN, L. & SANDHAM, N.D. 2006 Effect of Mach number on the structure of turbulent spots. *J. Fluid Mech.* **566**, 225–234.

VAN LEER, B. 1979 Towards the ultimate conservation difference scheme V, a second-order sequel to Godunov's method. *J. Comput. Phys.* **32**, 101–136.

LEES, L. & LIN, C.C. 1946 Investigation of the stability of the laminar boundary layer in a compressible fluid. *NACA Tech note No.* 1115.

LUMLEY, J.L. 1967 The structure of inhomogeneous turbulent flows. In *Atmospheric Turbulence and Radio Wave Propagation* (ed. A. M. Yaglom & V. I. Tatarski), pp. 166–178. Nauka.

MA, Y. & ZHONG, X. 2003 Receptivity of a supersonic boundary layer over a flat plate. Part 1. Wave structures and interactions. *J. Fluid Mech.* **488**, 31–78.

MACK, L.M. 1975 Linear stability theory and the problem of supersonic boundary-layer transition. *AIAA J.* **13** (3), 278–289.

MACK, L.M. 1984 Boundary-layer linear stability theory. *AGARD Rep.* 709.

MACK, L.M. 1990 On the inviscid acoustic-mode instability of supersonic shear flows. *Theor. Comput. Fluid Dyn.* **2** (2), 97–123.

NOVIKOV, A.V. 2017 Direct numerical simulation of transitional boundary layer with local separation in hypersonic flight. *7th European Conference for Aeronautics and Space Sciences (EUCASS)*. DOI: 10.13009/EUCASS2017-656.

NOVIKOV, A., EGOROV, I. & FEDOROV, A. 2016 Direct numerical simulation of wave packets in hypersonic compression-corner flow. *AIAA J.* **54** (7), 2034–2050.

PARK, S. & LAUCHLE, G.C. 2009 Wall pressure fluctuation spectra due to boundary-layer transition. *J. Sound Vib.* **319** (3-5), 1067–1082.

PULLIAM, T.H. & CHAUSSEE, D.S. 1981 A diagonal form of an implicit approximate-factorization algorithm. *J. Comput. Phys.* **39** (2), 347–363.

REDFORD, J.A., SANDHAM, N.D. & ROBERTS, G.T. 2012 Numerical simulations of turbulent spots in supersonic boundary layers: effects of Mach number and wall temperature. *Prog. Aerosp. Sci.* **52**, 67–79.

RESHOTKO, E. 1976 Boundary-layer stability and transition. *Annu. Rev. Fluid Mech.* **8** (1), 311–349.

ROE, P.L. 1981 Approximate Riemann solvers, parameter vectors and difference schemes. *J. Comput. Phys.* **43**, 357–372.

SALEMI, L.C. & FASEL, H.F. 2018 Synchronization of second-mode instability waves for high-enthalpy hypersonic boundary layers. *J. Fluid Mech.* **838**, R2.

SAYADI, T., HAMMAN, C.W. & MOIN, P. 2013 Direct numerical simulation of complete h-type and k-type transitions with implications for the dynamics of turbulent boundary layers. *J. Fluid Mech.* **724**, 480–509.

SHADLOO, M.S. & HADJADJ, A. 2017 Laminar-turbulent transition in supersonic boundary layers with surface heat transfer: a numerical study. *Numer. Heat Trans.* A *Appl.* **72** (1), 40–53.

SHU, C.W. & OSHER, S. 1988 Efficient implementation of essentially non-oscillatory shock-capturing schemes. *J. Comput. Phys.* **77** (2), 439–471.

SIROVICH, L. 1987 Turbulence and the dynamics of coherent structures. I. Coherent structures. *Q. Appl. Math.* **45** (3), 561–571.

SIVASUBRAMANIAN, J. & FASEL, H. 2010 Numerical investigation of boundary-layer transition initiated by a wave packet for a cone at mach 6. *48th AIAA Aerospace Sciences Meeting Including the New Horizons Forum and Aerospace Exposition. AIAA Paper* 2010-0900.

SOUDAKOV, V.G., EGOROV, I.V., FEDOROV, A.V. & NOVIKOV, A.V. 2016 Numerical simulation of receptivity and stability of a supersonic boundary layer. In *27th International Congress of the Aeronautical Sciences*.

STETSON, K.F. & KIMMEL, R. 1992 On hypersonic boundary-layer stability. *30th Aerospace Sciences Meeting and Exhibit, Reno, NV. AIAA Paper* 1992-737.

STETSON, K.F., THOMPSON, E.R., DONALDSON, J.C. & SILER, L.G. 1989 Laminar boundary layer stability experiments on a cone at mach 8, Part 5: tests with a cooled model. *20th Fluid Dynamics, Plasma Dynamics and Lasers Conference, Buffalo, NY. AIAA Paper* 1989-1895.

TUMIN, A. 2020*a* Lst and the eigenfunction expansion method for linearized navier-stokes equations–a summary. *AIAA Scitech 2020 Forum. AIAA Paper* 2020-0105.

TUMIN, A. 2020*b* Wave packets and supersonic second modes in a high-speed boundary layer. *AIAA Scitech 2020 Forum. AIAA Paper* 2020-0106.

UNNIKRISHNAN, S. & GAITONDE, D.V. 2016 Acoustic, hydrodynamic and thermal modes in a supersonic cold jet. *J. Fluid Mech.* **800**, 387–432.

UNNIKRISHNAN, S. & GAITONDE, D.V. 2018 Transfer mechanisms from stochastic turbulence to organized acoustic radiation in a supersonic jet. *Eur. J. Mech. (*B*/Fluids)* **72**, 38–56.

UNNIKRISHNAN, S. & GAITONDE, D.V. 2019*a* First-mode-induced nonlinear breakdown in a hypersonic boundary layer. *Comput. Fluids* **191**, 104249.

UNNIKRISHNAN, S. & GAITONDE, D.V. 2019*b* Interactions between vortical, acoustic and thermal components during hypersonic transition. *J. Fluid Mech.* **868**, 611–647.

WRIGHT, R. & ZOBY, E. 1977 Flight boundary layer transition measurements on a slender cone at Mach 20. *10th Fluid and Plasmadynamics Conference. AIAA Paper* 1977-719.

WYGNANSKI, I., SOKOLOV, M. & FRIEDMAN, D. 1976 On a turbulent 'spot' in a laminar boundary layer. *J. Fluid Mech.* **78** (4), 785–819.

WYGNANSKI, I., ZILBERMAN, M. & HARITONIDIS, J.H. 1982 On the spreading of a turbulent spot in the absence of a pressure gradient. *J. Fluid Mech.* **123**, 69–90.

YATES, H.B., TUFTS, M.W. & JULIANO, T.J. 2020 Analysis of the hypersonic cross-flow instability with experimental wavenumber distributions. *J. Fluid Mech.* **883**, A50.

ZHANG, S., LIU, J. & LUO, J. 2016 Effect of wall-cooling on mack-mode instability in high speed flat-plate boundary layers. *Z. Angew. Math. Mech.* **37** (9), 1219–1230.